Quantum simulation: from fractals to topological insulators

Albert J. Pool
Theoretical Physics

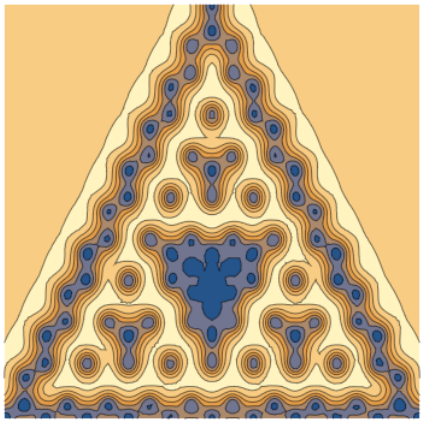

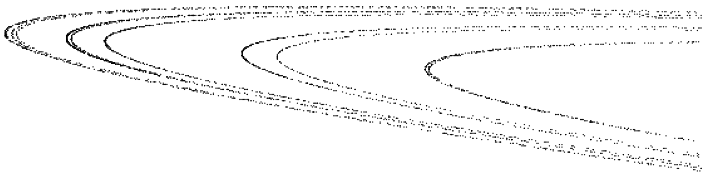

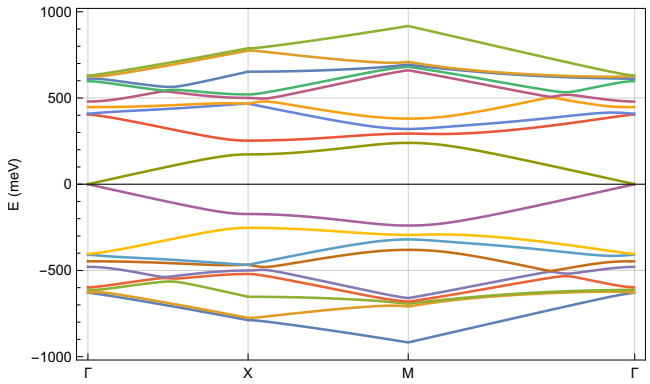

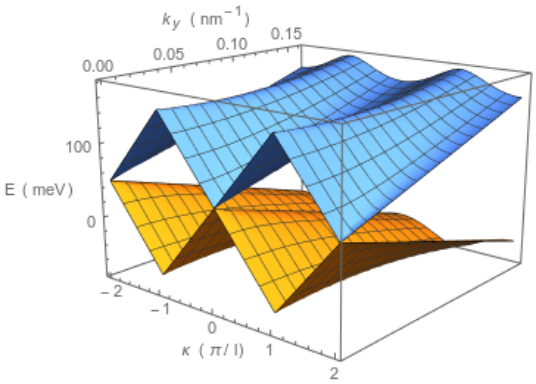

Supervisors:
Prof. Dr. Cristiane Morais Smith
Sander N. Kempkes MSc
Institute for Theoretical Physics, Universiteit Utrecht

Dr. Dario Bercioux
Donostia International Phyics Center, San Sebastián

A thesis presented for the degree of Master of Science
June 2019

Universiteit Utrecht

Cover images:
Local density of states in an electronic Sierpiński triangle at -325 meV, detail picture of an Hénon attractor after 5×10^5 iterations.
Band structure of a topological insulator with (left) out-of-plane magnetic nanoparticles and an average magnetic field of zero, (right) quasi-1D electrostatic barriers.

Contents

1 Introduction **1**

2 Quantum simulations **3**
2.1 Cold atoms 4
2.2 Photonics 5
2.3 Electronic quantum simulators 5
2.3.1 Bottom-up: colloidal nanocrystals 5
2.3.2 Top-down: 2D electron gases 6
2.4 Muffin tin method 7
2.5 Experiment 8
2.6 The Lieb lattice 10

3 Fractals **13**
3.1 Sierpiński triangle 14
3.2 Results 15

4 Multifractality **19**
4.1 Results for fractals 21
4.2 Results for electronic states in fractals 23

5 Three-dimensional topological insulators **25**
5.1 Transfer matrix method for single barriers 27
5.1.1 Electrostatic potential 29
5.1.2 Out-of-plane magnetic field 31
5.1.3 In-plane magnetic field 32
5.1.4 Delta barrier 34
5.2 Multiple barriers and periodic systems 37
5.2.1 Band structure and the Bloch theorem 37
5.2.2 2D systems 38
5.2.3 Results for quasi-1D 41
5.2.4 Results for 2D: muffin tin 42
5.2.5 The role of the 0th Fourier component 47

6 Conclusions and outlook **49**

Chapter 1

Introduction

In this thesis I will discuss different types of quantum simulation, focusing on simulation of two-dimensional systems. I will start with an introduction into quantum simulation in chapter 2, describing different methods before focusing on two-dimensional (2D) electron gases. From there on, the thesis basically consists of two parts, on surface states of metals and surface states of topological insulators.

In chapter 3 I will discuss an electronic fractal built using the surface electrons of copper. Many lattices have already been built using carbon monoxide molecules on copper [1–3]. Recently, it was shown by Kempkes et al. [4] that it is possible to confine electrons into a fractal structure and measure the fractal dimension of the electron wave function. The fractal used in that case is the Sierpiński triangle; in the related Sierpiński carpet, quantum transport, topological phases and Hall conductivity have been studied [5–7].
I will first replicate some results from the Sierpiński triangle to become acquainted with the technique and the concept of fractal dimension, and then generalise this to study multifractals in chapter 4: a fractal in which different parts have a different dimension, as opposed to a monofractal, which has the same fractal dimension anywhere and at any length scale. Multifractality has been predicted in electronic states of systems featuring a transition to/from a state with Anderson localisation [8], and an example system in which this has been found is a quantum Hall system at the transition between Landau levels [9]. As such, it is interesting to study whether multifractality can be observed in other electronic systems. I will do this for the electronic Sierpiński triangle, to find out whether the electrons confined to this monofractal form a monofractal themselves.

In the last part of the thesis, in chapter 5, I will introduce a three-dimensional topological insulator (3D TI) as a new material to simulate 2D fermions. 3D TIs are insulating in the bulk but conducting on the surface and this conduction comes from surface states, which form a 2D electron gas. As opposed to the surface electrons of copper, these surface states are massless Dirac fermions, having some similarities with the electrons in graphene. Unlike graphene however, these surface states are helical: spin is locked to momentum [10, 11]. This can be used to manipulate their electronic properties in new ways, for instance by introducing magnetic nanoparticles that act on the spin and the momentum of the surface states. I will study the electronic properties of these surface states using various kinds of potentials, to explore the possibilities that 3D TIs offer when nanoparticles are placed on top of them. Many of these potentials have already been studied using graphene [12–15], and it has been shown that a magnetic barrier can be

used to manipulate the current on a TI surface [16].
I will give an overview of the different types of potentials and discuss their similarities and differences with graphene. For each type of potential, I will calculate the transmission through a quasi-1D barrier and the band structure of a square lattice in 2D, to explore the different ways in which the surface states can be manipulated.

Chapter 2

Quantum simulations

> I want to talk about the possibility that there is to be an *exact* simulation, that the computer will do *exactly* the same as nature.
>
> Richard P. Feynman, 1981 [17]

Quantum mechanics is the physical theory describing the behaviour of particles on the scale of single atoms. It has successfully explained various systems such as the electron states of the hydrogen atom. However, as systems get larger and include more particles, it quickly becomes impossible to provide exact solutions. For this reason, theorists try to study quantum mechanical systems by simulating them. This task is impractical on a classical computer because the amount of computing power required grows exponentially as the system size increases. In 1981, Richard Feynman came up with the idea to simulate quantum systems using *another* quantum system [17].

Feynman envisioned quantum computers to perform these simulations, but quantum computers outperforming traditional ones have not yet been made. Still, it is possible to simulate a quantum system, by using a purpose-made simulator instead of a general quantum computer [18]. In the next section, I will discuss various methods to simulate two-dimensional electronic systems, before introducing the simulation method used in this thesis.

The goal of a quantum simulation is usually to build a system that has the same degrees of freedom as the simulated system, but at a (much) larger scale, which makes it is easier to manipulate [19]. In this chapter, I will give a number of examples of quantum simulators of 2D condensed matter systems. Cold atoms, photonic or electronic simulators can be used to simulate spin systems with nearest-neighbour interactions, and to reproduce the electronic band structure of various lattices. I will then go on to describe the simulator of 2D electrons used in the following chapters.

2.1 Cold atoms

Ultracold atoms can be confined in an optical lattice to simulate a condensed-matter system. An optical lattice is created by using counter-propagating lasers: for instance, two sets of lasers in the x- and y-direction are required for a 2D square lattice [20]; 3 lasers at angles of 120° for a triangular lattice [21], or three sets of lasers in the x-, y-, and z-directions for a 3D square lattice [22]. An example of 2D and 3D square optical lattices can be seen in figure 2.1.

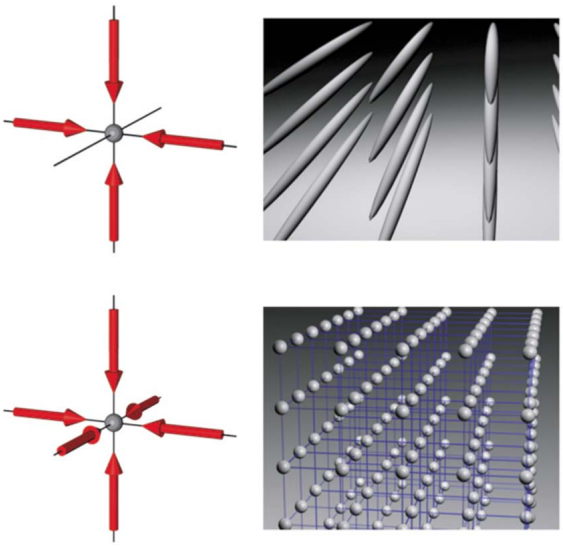

Figure 2.1: Optical lattices in 2D (top) and 3D (bottom). From Bloch et al. [22].

This optical lattice forms a defect-free potential whose lattice constant is determined by the wavelength of the lasers. In this potential, fermions or bosons can be placed; their interactions can be controlled by Feshbach resonances, which can be used to induce attractive or repulsive interactions in certain atomic species by applying a magnetic field. In particular, a repulsive interaction can be used to trigger a phase transition for bosons from a superfluid to a Mott insulator [23]. Other possible applications include simulating spin systems such as the quantum Ising model [23] and topological insulators [24].

Another possible cold atom simulation can be made using a Fermi gas: a gas of fermions in which all quantum states are occupied up to the Fermi level. The interactions between these atoms can be tuned by Feshbach resonances too. Attractive interactions will lead the fermions to form (bosonic) pairs; in the case of weak interactions, these are Cooper pairs leading to superfluidity as described by BCS theory. In the case of strong interactions these bosons form a Bose–Einstein condensate [23].

There are much more possibilities to use cold atoms in simulations. For instance Anderson localisation can be simulated using a disordered optical potential [25, 26], a rotating Fermi gas can be used to simulate a quantum Hall system [23], ions in radiofrequency traps can be used to simulate magnetic systems on a lattice [27], and cold atoms on an optical lattice can be applied to high-energy physics, simulating lattice gauge theories [28].

2.2 Photonics

Photons can be easily guided using waveguides and do not interact much. This means that they can be moved without much decoherence, so they can be used to simulate a lattice without actually being confined to it. Interactions are modelled by generating superpositions of two photon beams using beam splitters. This results in interference between the beams which can be measured in a detector at the end of the circuit. As photons are bosonic, these simulators are well suited to simulating bosons. A schematic example of a photonic simulator can be seen in figure 2.2.

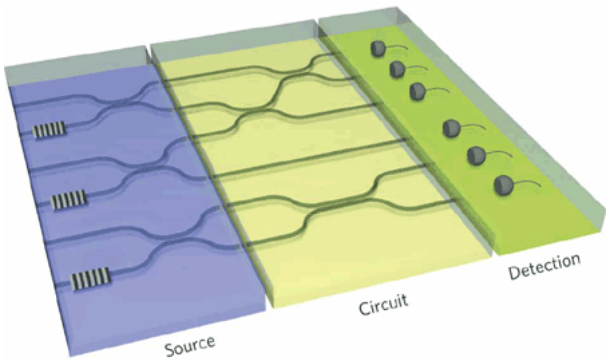

Figure 2.2: An example of a photonic simulator. From Aspuru-Guzik and Walther [30].

Using relatively simple optical setups, systems of interacting spins can be simulated. This has been demonstrated for a 4-atom frustrated Heisenberg system [29]. Apart from spin systems, applications of photonic systems are foreseen in particle physics [30]. Topological edge states can be found in photonic crystals with periodic modulation, so-called Floquet time crystals [31], or by simulating a quantum Hall system in a magnetic field [32].

2.3 Electronic quantum simulators

Like bosons can be simulated using photons, fermions can be simulated using electrons. It is well possible for instance, to simulate an electronic system on a lattice by building a similar lattice on a different scale. This can be used to find the electronic properties of the simulated system. Compared to simulators based on cold atoms and photonic simulators, electronic simulators are still rather new. So far, it has mainly been used to build various two-dimensional lattices artifically, to simulate the behaviour of electrons on these kinds of lattices in condensed-matter systems.

Here, I will discuss a number of examples of electronic simulators, which I will divide into *bottom-up* approaches, where a lattice is assembled by placing particles on lattice sites and *top-down* approaches, where a lattice is created by confining electrons to lattice sites.

2.3.1 Bottom-up: colloidal nanocrystals

From lead chalcogenides (PbS, PbSe, or PbTe), colloidal particles can be formed, which have the shape of truncated nanocubes. These colloids can self-assemble into a lattice, in which they take the place of atoms, hence characterising a bottom-up approach.

Possible lattices using this type of colloid are a square lattice or a buckled honeycomb-like "silicene" lattice. These colloidal systems exhibit electronic bands resembling those of graphene, and interesting topological states due to spin-orbit coupling have been theoretically predicted [33, pp. 44–56, 34, 35, 36]. An example of such a system can be seen in figure 2.3.

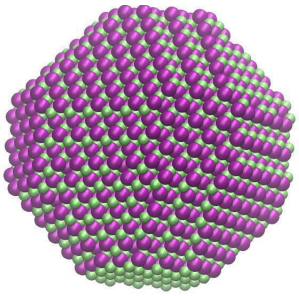

(a) Example of a truncated nanocube. From Tadjine [33, p. 44].

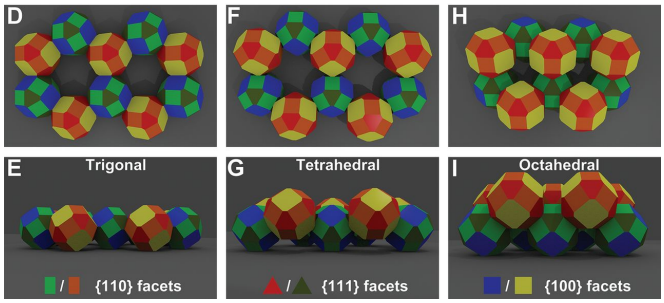

(b) Examples of hexagonal crystal structures of truncated nanocubes. From Boneschanscher et al. [35].

Figure 2.3: Colloidal nanoparticles self-assembled into a crystal.

2.3.2 Top-down: 2D electron gases

A 2D electron gas is formed by confining an electronic system in one direction, for instance by using a thin film of a (semi-)conducting material, or the surface states of a topological insulator. In these systems, electrons can be confined even further to form an artificial lattice, hence this is a top-down approach. Many experiments with 2D electron systems were done after it was theoretically shown that graphene can be simulated by patterning a 2D electron gas [37]. Here I will present some examples of 2D electron systems, which have been built experimentally to model various lattices.

Semiconductors

Electrons can form a 2D electron gas on the boundary of a thin semiconducting film in the presence of a dopant. These electrons can be confined by etching holes into the system. This approach has been demonstrated using AlGaAs or GaAs with a triangular pattern to build an artificial graphene lattice. This method allows simulating localised as well as delocalised electronic states [38] and massless Dirac fermions [39–41]. The lattice constant in these simulations is usually in the range 50–150 nm.

Metals

In metals such as copper, there are surface states that form a 2D electron gas. In such a system, electrons can be confined to a lattice either by creating vacancies in the surface, or by building nanostructures on top of the surface. The properties of such structures can be measured using STM. Lattice constants in the order of 2 nm are well possible in these systems, much smaller than in semiconductors.

Vacancies in a Cu(100) surface have recently been used to model the Lieb lattice [42], which is a square lattice with some missing sites that I will describe in section 2.6. Carbon monoxide molecules adsorbed on Cu(111) have been used as well to model this lattice,

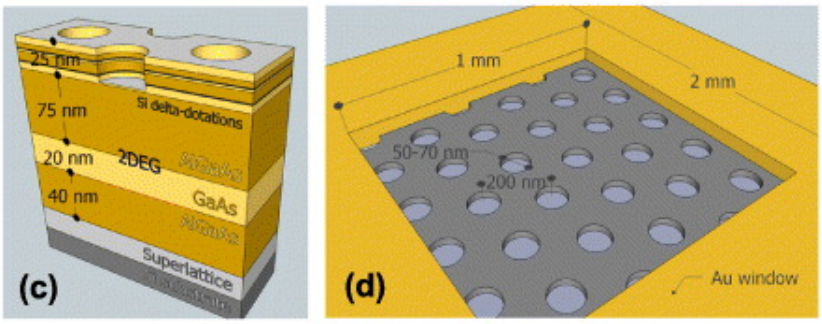

Figure 2.4: Example of a graphene lattice on a semiconductor surface. From Nádvorník et al. [40].

and other lattices such as the graphene lattice [1]. Recently a fractal was simulated: the Sierpiński triangle [4], which I will describe in chapter 3.

It has also been shown that quantum simulation with CO molecules on a Cu(111) surface can reproduce the atomic s- and p-orbitals of atoms in a graphene or Lieb lattice. In a Lieb lattice geometry the p_x- and p_y-orbitals can even be manipulated separately [3]. These recent developments open up many possibilities for simulating 2D electronic systems [43], coming a step closer to the universal quantum simulator envisioned by Feynman.

Topological insulators
Three-dimensional topological insulators feature surface states that behave as a massless 2D electron gas. Like the edge states of two-dimensional topological insulators [44], these surface states are *helical*, which means that they have a spin locked to their momentum [10, 11].

These materials are still relatively new, having been theoretically predicted in 2007 [45] and experimentally detected in 2009 [11]. Some experiments have been set up to pattern a topological insulator by doping with, or adsorbing iron atoms [46, 47]. It has been suggested that the helical property of the surface states can be used for *spintronics*: electronics driven by spin currents instead of charge currents [48, 49].

In chapter 5, I will explore the possibilities of patterning a topological insulator surface with different kinds of nanoparticles, and compare the TI surface states with the massless Dirac fermions of graphene, which are not helical.

2.4 Muffin tin method

In this section, I will give a theoretical description of surface electrons, confined by patterning the surface using nanoparticles. This confinement generates artificial atomic sites, of which the occupancy can be modelled using either a muffin tin potential, or a tight-binding model [1, 2, 4].

I will describe the muffin tin potential here: a potential that has a nonzero value V within a radius r around the particle, and is zero anywhere else. When drawn in 3D using a square lattice, this potential resembles an upside-down muffin tin. The parameters V and

r depend on the properties of the nanoparticles; to describe CO molecules on a Cu(111) surface, I will use $V = 0.9$ meV and $r = 0.3$ nm. The surface states themselves are described by the Schrödinger equation with an effective mass $m^* = 0.42\ m_e$ [50]. The Hamiltonian is then given by

$$H = -\frac{\hbar^2}{2m^*}\nabla^2 + V_{\mathrm{CO}}(\vec{r}), \tag{2.1}$$

with $V_{\mathrm{CO}}(\vec{r})$ the muffin tin potential as described.

Solving the Schrödinger equation numerically in this system results in a set of electron eigenfunctions and their respective energies. For the binding energy, -0.45 eV is used; this value is added to the energy levels of the surface states. Experimentally this is known to be -445 meV [51]. A Lorentzian broadening of $\Gamma = 0.08$ eV is applied to the calculated eigenenergies to calculate the local density of states (LDOS) because interactions with the bulk of the metal cause surface states to be broadened [1]. The LDOS can be plotted at a fixed position/lattice site as a function of energy, or at a fixed energy as function of position, which is called an LDOS map. All parameters mentioned here are in line with Kempkes et al. [4] to allow comparison with existing results.

Later, in section 5.2.4, I will apply a similar potential on top of a gas of massless Dirac fermions to study surface states of topological insulators.

2.5 Experiment

This system of CO molecules adsorbed on a copper surface can be studied experimentally using a scanning tunneling microscope (STM). Using the tip of an STM, one can pick up CO molecules and arrange them in a lattice, and then use the STM to measure the LDOS of the resulting system. This method has been described before by Gomes et al. [1].

The tunnelling current between the tip of the STM and the surface is proportional to the number of conducting states below the Fermi level. This level is determined by the voltage applied between the tip and the substrate. The density of states at a certain voltage is then found by taking the derivative of the current to the voltage, also called the *differential conductance* $\frac{\mathrm{d}I}{\mathrm{d}V}$.

These spectra depend greatly on the tip of the STM, and for that reason they need to be *normalised* using the $\frac{\mathrm{d}I}{\mathrm{d}V}$ spectrum of a clean copper surface. By dividing the spectrum of a lattice site by that of clean copper, one "divides out" the effects caused by the tip and the copper bulk, and the result is a normalised spectrum that can be seen as an experimental LDOS.

An example of this procedure can be seen in figure 2.5. It shows the $\frac{\mathrm{d}I}{\mathrm{d}V}$ spectrum at a certain lattice site for three different tips, before and after normalisation, and the main features of this spectrum are present with all tips. These figures come from an experiment on the Sierpiński triangle [4], which will be described in section 3.1. However to understand the procedure of normalisation it is not necessary to know the details of the lattice structure.

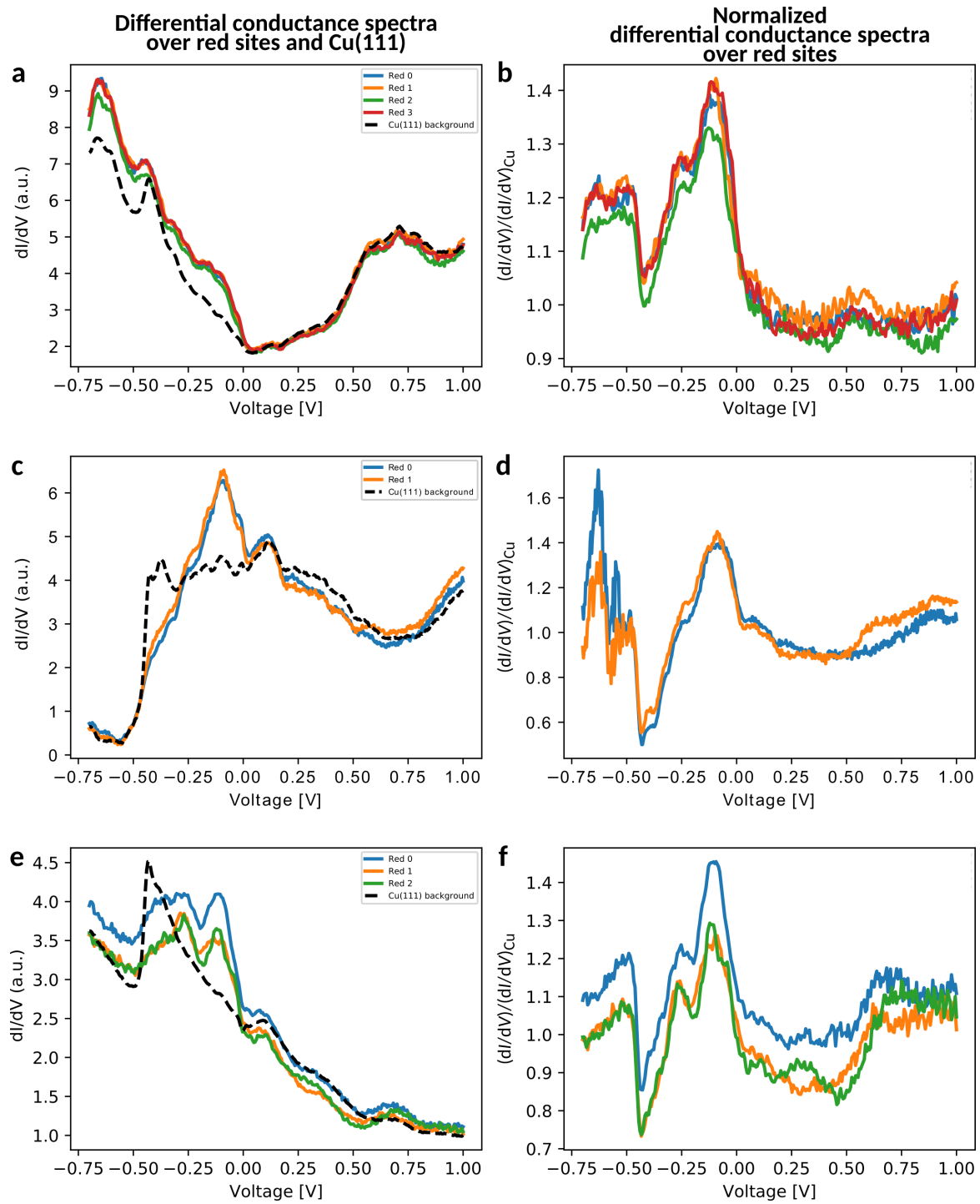

Figure 2.5: (a,c,e) The differential conductance spectrum of a clean copper surface (dashed) compared with that of a number of equivalent sites in the third generation Sierpiński triangle, for three different STM tips. (b,d,f) The corresponding normalised spectrum for the same sites and tips. From Kempkes et al. [4], supplementary material.

2.6 The Lieb lattice

To become acquainted with the method, I first show the results for the Lieb lattice, which had already been studied before by Slot et al. [2]. Here, I reproduce their muffin-tin calculations and compare them with their experimental results.

The Lieb lattice is depicted in figure 2.6a. It is a variation on the square lattice; in the unit cell of 2×2 particles, one of the four is missing. This leads to a lattice in which there are particles with four neighbours ("corner sites" shown in blue in the figures) or two neighbours ("edge sites" in red). This lattice is interesting to study as it is a common feature of high-T_c superconductors based on CuO_2 [52].

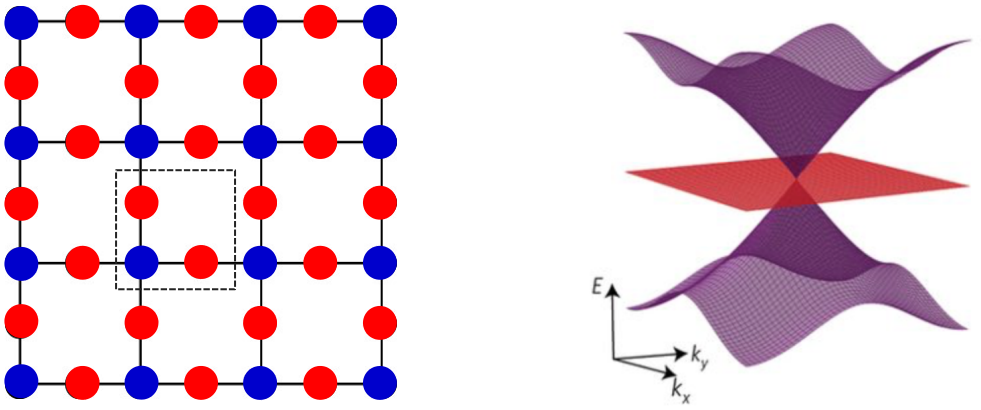

(a) The lattice with corner sites in blue and edge sites in red. The dotted line marks one unit cell.

(b) The band structure around the M point of the Brillouin zone.

Figure 2.6: The Lieb lattice and its band structure.

The Lieb lattice is one of the simplest lattices featuring sites with different connectivity. When taking only nearest-neighbour hopping into account, it has a Dirac cone around the M point of the Brillouin zone and a flat band through the Dirac point, as can be seen in figure 2.6b. This flat band becomes dispersive when introducing next-nearest-neighbour hopping, which plays a significant role in this electronic Lieb lattice [2].

The muffin-tin potential used to study this lattice consists of 5×5 unit cells of 2.66×2.56 nm each; this difference between width and length follows from the underlying FCC lattice structure of the copper substrate, which dictates at which sites CO molecules can be placed. The placement of CO molecules on the substrate can be seen as black dots in figure 2.7 and the potential can be seen in figure 2.8.

For infinite periodic systems, the Bloch theorem tells us that the wave functions will be periodic with a phase difference between neighbouring unit cells [53, pp. 137-138]. The experimental system however has a finite size. Numerically it is also easier to solve the Schrödinger equation with periodic boundary conditions without a phase difference. I have taken a size of 5×5 unit cells, which is roughly comparable to the experimental system. Later, in section 5.2.2, I will use the Bloch theorem to describe an infinite system on a 3D topological insulator surface.

The LDOS for edge and corner sites is depicted in figure 2.9. In this figure, one can see

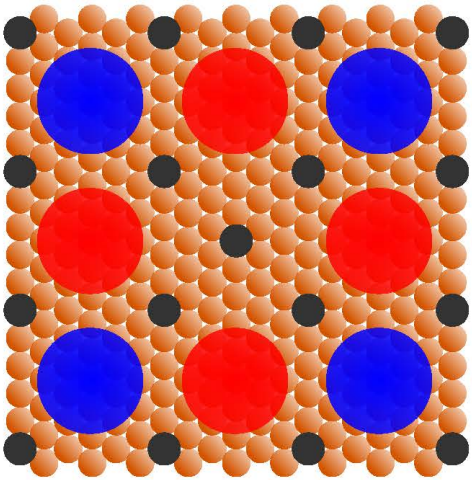

Figure 2.7: The placement of CO molecules (black) on top of a Cu(111) surface, to confine the surface electrons to the red and blue states. From Slot et al. [2].

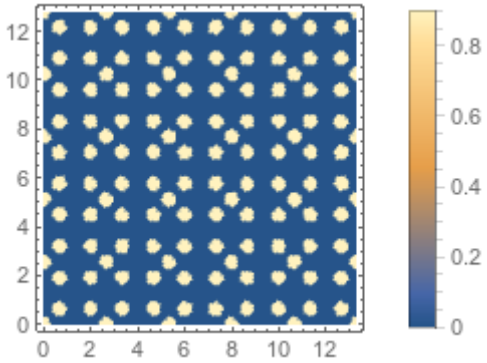

Figure 2.8: The muffin tin potential used to study the Lieb lattice. Scale in nm, colour: potential in eV.

that around −200 meV both intensities are roughly equal; around −50 meV the intensity at edge sites peaks and around +150 meV the intensity at corner sites peaks, which means that these are interesting energies to study the Lieb lattice system. At these energies, I have plotted the LDOS map of the system, which can be seen in figure 2.10. When comparing the data with STM data from Slot et al. [2], one can observe a clear similarity.

The energies given in electronvolt can be equated to the tension in volt between the needle and substrate in an STM, because the electronvolt is defined as the energy acquired by an electron charge moving through a potential difference of 1 V. This allows comparing the experimental and theoretical results.

As expected from figure 2.9, one can observe that electrons are localised on edge sites in figure 2.10b and on corner sites in figure 2.10c. There is a very good agreement between the calculated and experimental LDOS.

This is just one example of a system where the muffin tin method works well to describe the electronic surface states of copper with adsorbed CO molecules and in this section I have shown that I can reproduce this calculation. I will use this method in the next chapters to study electrons in fractal geometries.

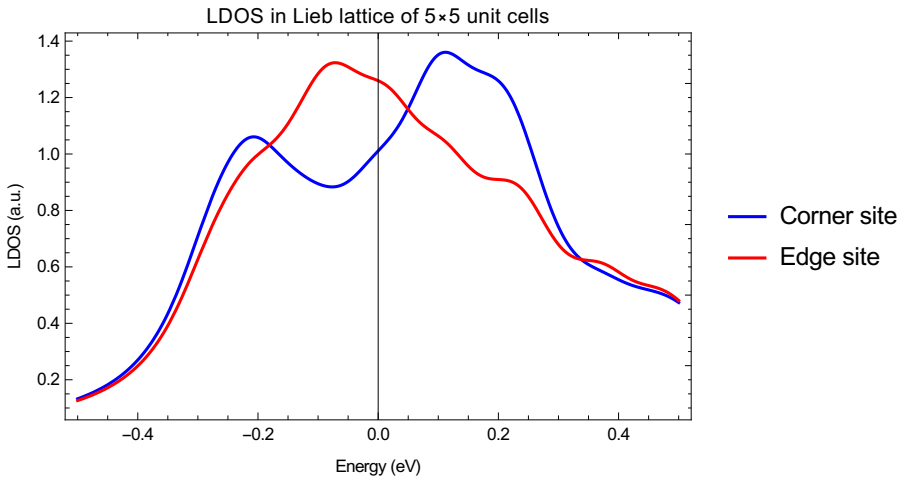

Figure 2.9: LDOS for edge and corner sites in the Lieb lattice, calculated using the muffin-tin method.

Muffin-tin

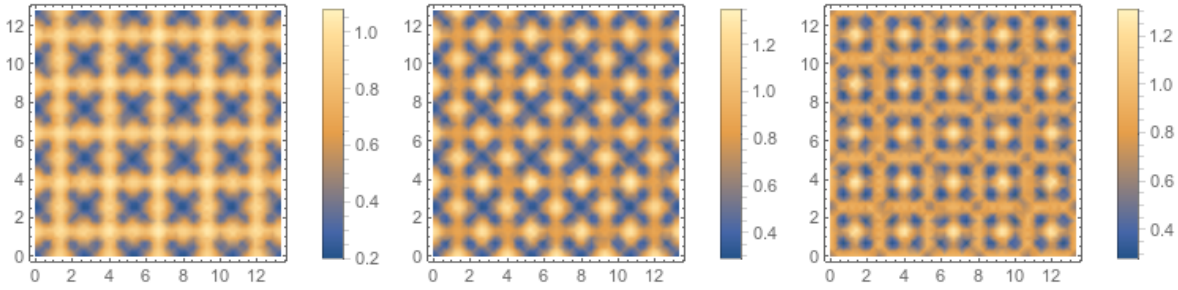

(a) $E = -200$ meV. (b) $E = -50$ meV. (c) $E = +150$ meV.

Experiment

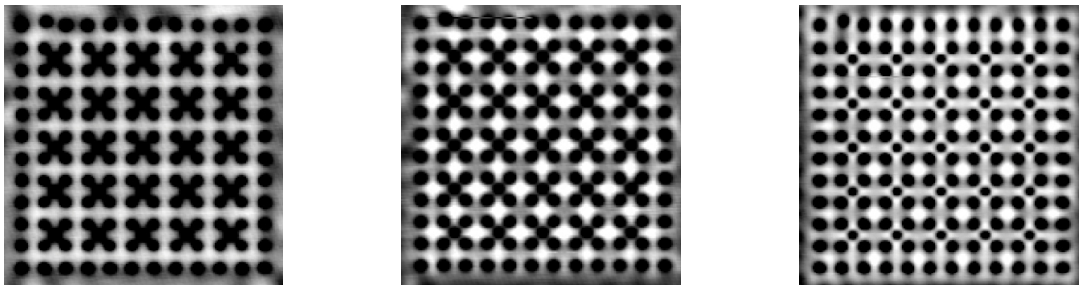

(d) $U = -200$ mV. (e) $U = -50$ mV. (f) $U = +150$ mV.

Figure 2.10: (a-c) LDOS map for various energies of a Lieb lattice of 5×5 unit cells, (d-f) experimental results of Slot et al. [2] at the corresponding potentials. The areas in yellow (white) have a high density of electronic states and the areas in blue (black) a low density.

Chapter 3

Fractals

> The left bank of the Vistula, when measured with increased precision, would furnish lengths ten, hundred and even thousand times as great as the length read off the school map.
>
> Hugo Steinhaus, 1954 [54]

Lengths of natural borders are hard to measure because they depend on the *scale* at which you are looking. This is true for the banks of the Wisła (or Vistula) river in Poland, but also for coastlines and land borders. It was in 1967, that Benoit Mandelbrot quantified this by measuring the *dimension* of the west coast of Britain [55].

The mathematical concept of this dimension was already defined in 1918 by Felix Hausdorff [56], who also proposed that it could be fractional. This *Hausdorff dimension* can be calculated as $D = \frac{\log N}{\log S}$, with N the number of copies of the fractal created by scaling the object by a factor S. It contrasts with the *topological* dimension D_T of an object which is always integer: zero for a point and one for a curve.

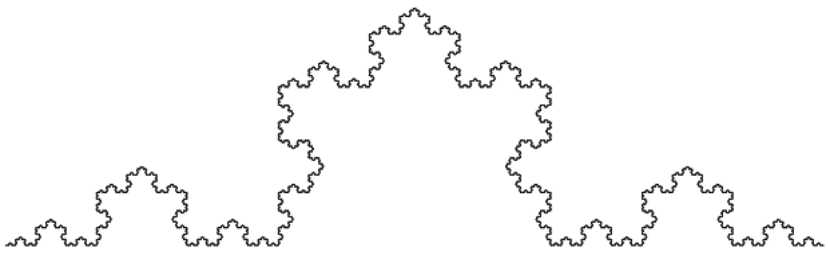

Figure 3.1: The Koch curve.

One of the earliest fractals to be developed was the *Koch curve* by Helge von Koch in 1904, at a time when the word *fractal* had not yet been introduced. The Koch curve is shown in figure 3.1. As a curve, its topological dimension is 1. The curve is obtained by iteratively taking the middle third of every line segment and replacing it by an outward pointing equilateral triangle, removing the original line segment at the base. The removed segment is thus replaced by two segments of the same length as the original. Every one iteration creates four copies of the previous curve at a size three times smaller; or, in other words, scaling the system to three times its size results in a curve length four times

longer, leading to a Hausdorff dimension $D = \frac{\log 4}{\log 3} \approx 1.26$ [57, pp. 34–38]. Combining three Koch curves, one gets the *Koch snowflake*. I will use the Koch curve later as an example in section 4.1.

In 1975, Mandelbrot [57, p. 15] used this dimension to define a fractal as *a set for which the Hausdorff Besicovitch dimension strictly exceeds the topological dimension.* This definition allows for a very broad range of fractals, and not everybody is comfortable with it because of a number of edge cases, which are by this definition a fractal, but lack some important properties that are found in other fractals. For instance, the *Peano curve* is a curve which fills the whole unit square, i.e. $D = 2$, $D_T = 1$ [57, p. 58]. Unlike the Koch curve, this square is very simple to describe geometrically and lacks structure at small scales. Because of these and other edge cases, Falconer came up with a "hand-waving" definition of a fractal [58, p. xxv]. By this definition, a fractal should at least:

- have a detailed structure at any length scale,
- be not easily described in geometric terms,
- have some sort of self-similarity,
- usually have a Hausdorff dimension D strictly greater than D_T,
- usually be described with a very simple, perhaps iterative, procedure.

The Koch snowflake complies with all of these and is thus by either definition a fractal. This also applies to the other fractals that I will discuss in this thesis, and I will not take a stand on which definition is "right".

Note that in either definition, it is not necessary that D is fractional even though the name *fractal* suggests so. The boundary of the well-known *Mandelbrot set*, for instance, has a Hausdorff dimension of 2 [59]. Following Mandelbrot, I will from now on use *fractal dimension* for the Hausdorff dimension of a fractal.

3.1 Sierpiński triangle

I will focus on one particular fractal known as the Sierpiński triangle, which can be seen in figure 3.2. This triangle was first described in a mathematical sense by Wacław Sierpiński in 1915, when he proved that it is *a curve on which every point is a branch point* [60].

The fractal, also called the Sierpiński gasket, is created iteratively from an equilateral triangle by dividing the triangle into 4 smaller ones, then taking out the middle triangle and repeating this procedure on the three remaining triangles. Repeating this process, the area tends to zero, and in the limit of infinitely many iterations one gets the curve as described by Sierpiński [57, p. 131].

The Sierpiński triangle was not an entirely new idea at the time: stuctures resembling the Sierpiński triangle can be found in medieval art [61], and the idea of having a (three-dimensional) structure with many branch points and different length scales was already used in architecture. Of course a structure of zero volume is not physical, but after a few iterations of "taking out triangles", one obtains a structure which is strong and has a small density, and as a result (relatively) lightweight. Such a structure is found in, for instance, the Eiffel tower [57, p. 131]. Nanomaterials with a three-dimensional structure

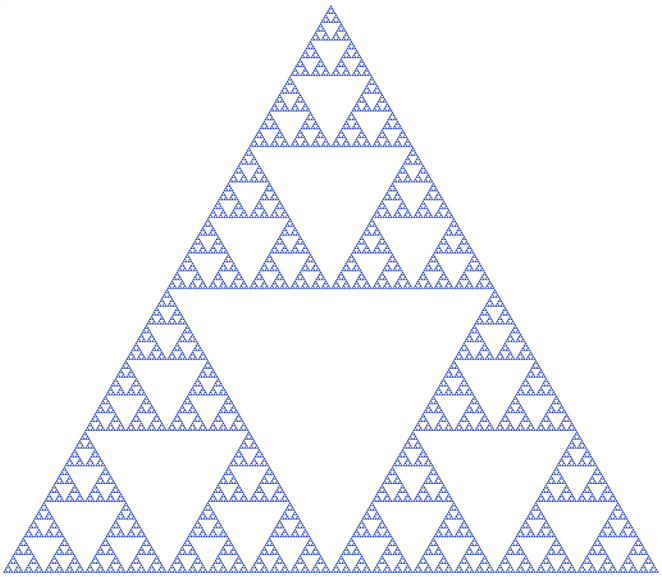

Figure 3.2: The Sierpiński triangle.

similar to the Sierpiński triangle have been produced experimentally, and these too have an extraordinary strength compared to their density [62]. Besides, such structures were envisioned as low-density building blocks for extraterrestrial technology in a semi-serious paper by Dyson [63] written for the 60th birthday of physicist Hans Bethe, which outlines how societies with more advanced space technology would probably look like.

Scaling the Sierpiński triangle by a factor of 2 results in three copies of the triangle, which means that the fractal dimension is $D = \frac{\log 3}{\log 2} \approx 1.58$. This is indeed greater than the topological dimension of a curve $D_T = 1$. Electrons in this fractal have already been studied by Kempkes et al. [4], and in the next section I will reproduce some of their results.

3.2 Results

I have applied the same muffin tin calculation as described in section 2.4, to the third-generation Sierpiński triangle. The boundary conditions are different as this system is not periodic in the x- or y-direction. For this reason I used Neumann boundary conditions setting the derivative of the wave function to zero at this boundary. I used a square system of 38×33 nm, which is twice the length and width of the Sierpiński triangle itself. I have done this to avoid creating lattice sites on the boundary of the system where electrons are confined between two Sierpiński triangles. The potential can be seen in figure 3.3.

First, I plotted the LDOS for sites with one, two or three neighbours. This can be seen in figure 3.4. It shows that the LDOS of different sites peaks at different energies.

Using this figure, four interesting energy levels are selected. At $E = -325$ meV all three kinds of sites show a roughly equal intensity; at -200 meV sites with one or two neighbours are accentuated and at -100 meV even more; at $+100$ meV sites with three neighbours are accentuated. The results for these energy levels can be seen in figure 3.5, compared with experimental data of Kempkes et al. [4].

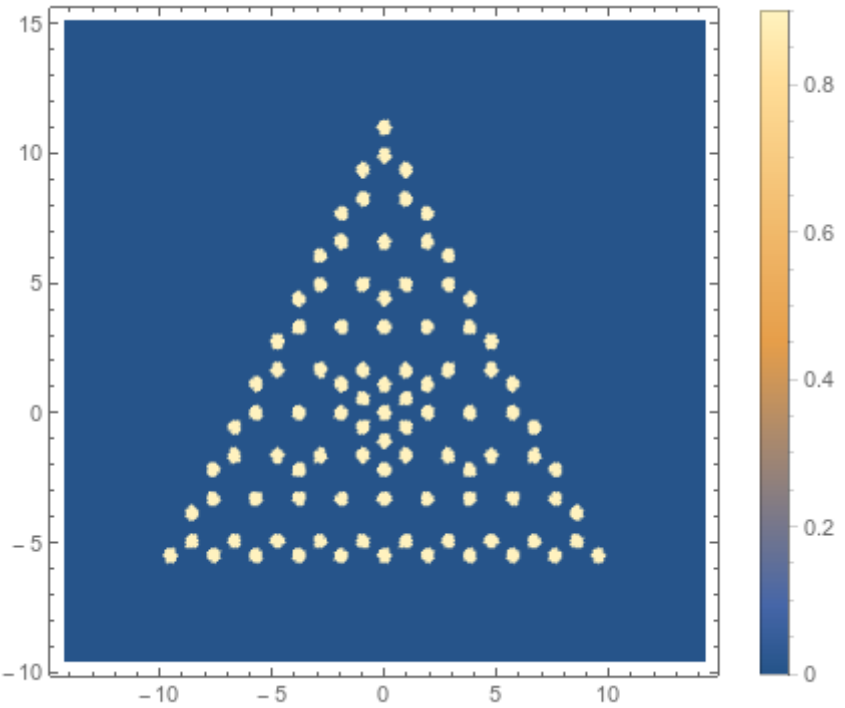

Figure 3.3: The muffin-tin potential used to study the Sierpiński triangle. Scale in nm, colour: potential in eV.

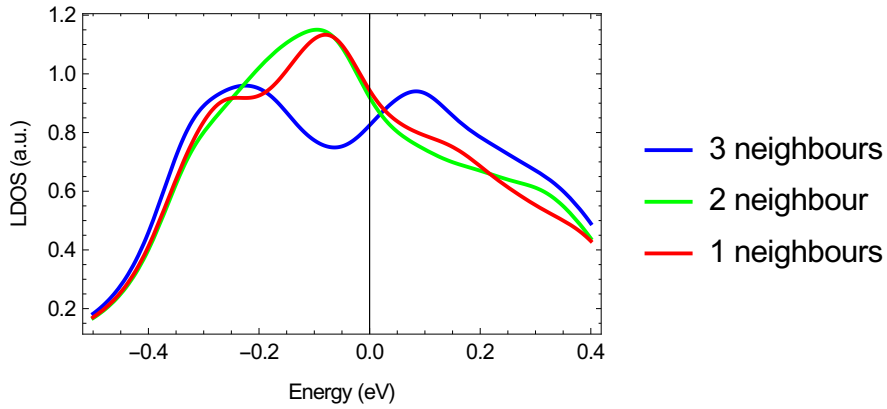

Figure 3.4: LDOS for the three different sites in the third generation Sierpiński triangle, calculated using the muffin-tin method.

(a) $E = -325$ meV, muffin tin.

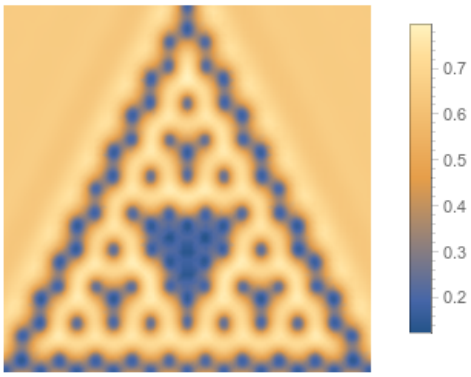

(b) $U = -325$ mV, experimental.

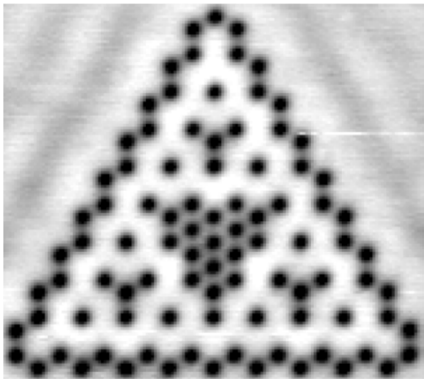

(c) $E = -200$ meV, muffin tin.

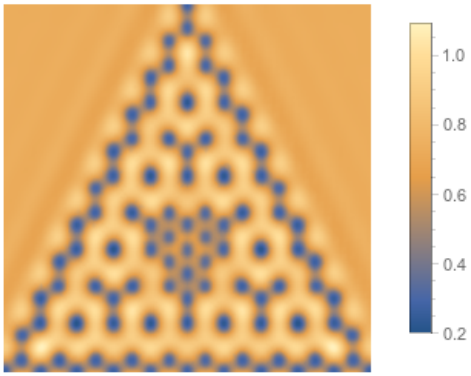

(d) $U = -200$ mV, experimental.

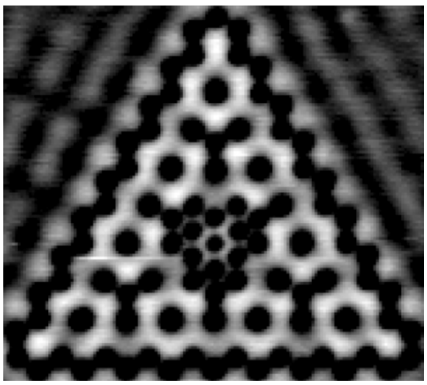

(e) $E = -100$ meV, muffin tin.

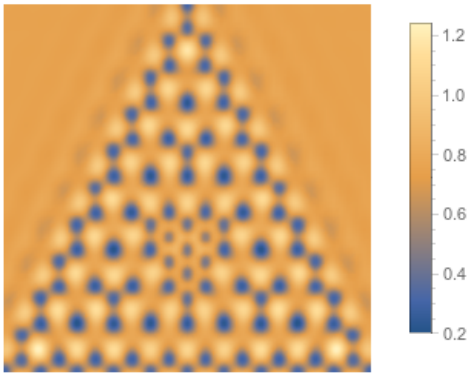

(f) $U = -100$ mV, experimental.

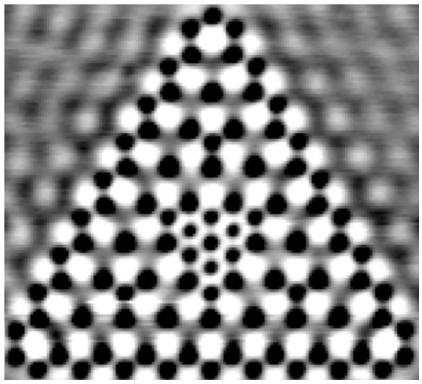

(g) $E = +100$ meV, muffin tin.

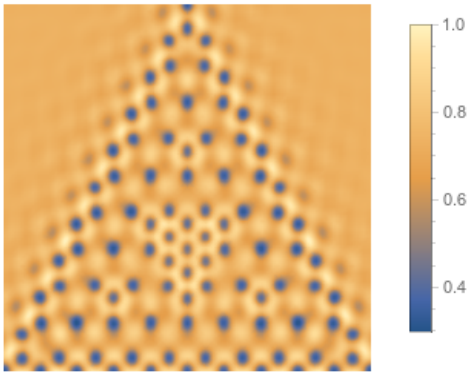

(h) $U = +100$ mV, experimental.

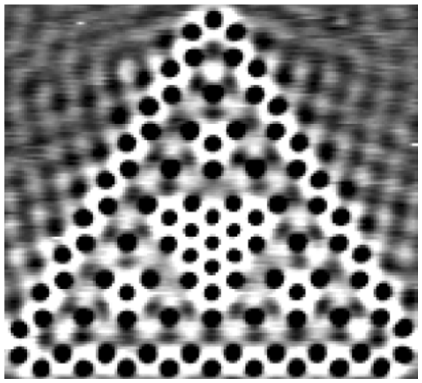

Figure 3.5: LDOS map of the Sierpiński triangle: (a,c,e,g) Muffin-tin calculations. (b,d,f,h) Experimental data from Kempkes et al. [4]. Same scale as figure 3.3.

The fractal nature of wave functions in this model of the Sierpiński triangle can be confirmed by analysing the Fourier transform of the LDOS maps. Figure 3.6 shows that this system exhibits self-similarity up to 3 levels: there is a threefold repetition in the Fourier spectrum, and one can retrieve the second- and first-generation Sierpiński triangle from the Fourier spectrum by removing the points with the highest momenta. This is as expected when studying the third generation of the fractal.

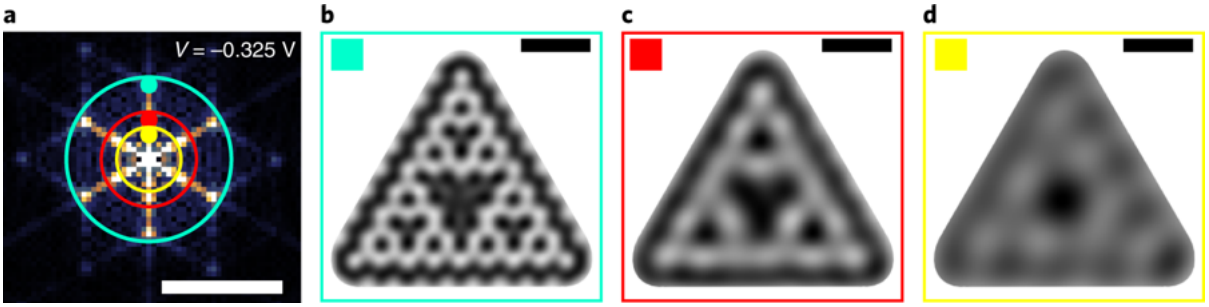

Figure 3.6: (a) Fourier transform of the experimental LDOS map at $U = -325$ mV shown in figure 3.5b. (b-d) Inverse transform of the Fourier spectrum inside the blue, red, and yellow circles of (a) respectively. (c) is similar to the second-generation Sierpiński triangle and (d) is similar to the first-generation Sierpiński triangle. From Kempkes et al. [4].

Determining the dimension of a fractal numerically can be done with the box counting method: counting the number of boxes necessary to cover the fractal, at different box sizes. The dimension is then found as

$$D = \lim_{r \to 0} \frac{\log N(L)}{-\log L}, \tag{3.1}$$

with $N(r)$ the number of boxes of length L necessary to cover the fractal [58, p. 43]. To apply this to an LDOS map, a cutoff has to be defined to determine whether a box is said to contain any part of the electronic fractal. Also, the range of box sizes used has to be chosen. As these parameters are rather arbitrary, this means that the results of box counting can vary. I have thus averaged $N(L)$ for a number of different cutoffs ranging from 60% to 90% of the maximum intensity of the LDOS map, using box sizes ranging from 50×50 to 500×500 pixels in an image of size 3500×3500. The results can be seen in table 3.1.

Energy (meV)	Dimension
-325	1.84 ± 0.017
-200	1.782 ± 0.023
-100	1.70 ± 0.04
+100	1.774 ± 0.023

Table 3.1: Box counting dimension of the LDOS map as a function of energy.

The dimension of the electronic fractal is higher than 1.58 but clearly between one and two. This is another indication that the electrons in this system are confined to a fractal. In the next chapter I will analyse the dimensionality of the system further by looking at multifractality.

Chapter 4

Multifractality

> Much of textbook mechanics concerns dynamical systems whose attractors are points, near-circles, or other shapes from Euclid. But these are rare exceptions, and the behavior of most dynamic systems is incomparably more complicated: their attractors or repellers tend to be fractals.
>
> Benoit B. Mandelbrot, 1982 [57, p. 195]

In the previous chapter, I introduced fractals that were very regular structures characterised by a particular fractal dimension. Fractality, however, can also be observed in less regular systems. In this section I will introduce the *multifractal*, an object that shows fractality under distortion. As a generalisation of the fractal with a single dimension D, it has a multifractal dimension D_q which is a function of the moment q. Studying multifractality is a powerful tool to analyse images in medicine [64] and geology [65].

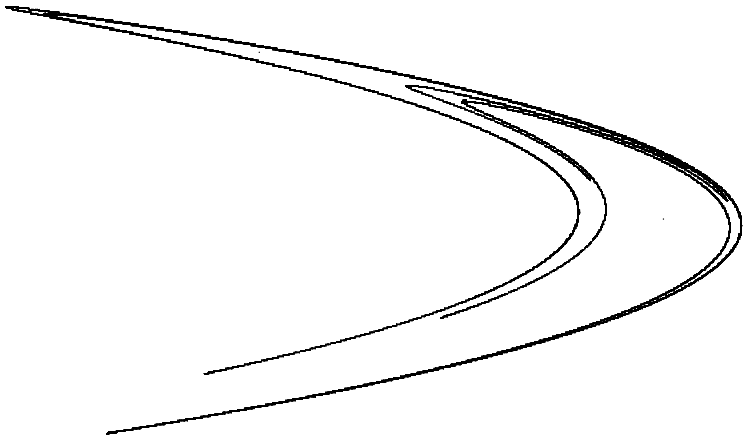

Figure 4.1: The Hénon attractor.

A good example of a multifractal is the Hénon attractor, shown in figure 4.1. It is formed from a dynamical system known as the Hénon map; for a given starting point in $\mathbb{R}^2$, this system evolves either to infinity or to a set of points known as the attractor. This attractor looks rather simple but it is not; the "curves" visible in the figure are actually sets of more-or-less parallel "curves" which themselves resemble a Cantor set [66]. A detail of this can be seen in figure 4.2. As such, it has a visible fractal structure at small scales, and it has a fractal dimension of $D = D_0 = 1.261 \pm 0.003$ [67].

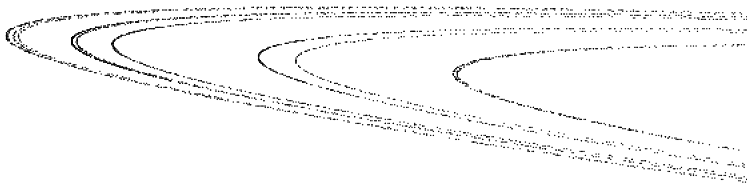

Figure 4.2: Detail of the Hénon attractor, 5×10^5 iterations.

At the end of the previous chapter I studied an electronic fractal, formed by confining electrons to the third generation of the Sierpiński triangle. From the Fourier spectrum and dimension, one could deduce that the electronic states resemble a fractal.

The Sierpiński triangle is a known monofractal, which has the same fractal dimension anywhere. In this chapter, I want to determine whether its electronic version has the same properties, or whether it is a multifractal containing components of different dimensions. This is interesting because multifractality has already been observed in electronic surface states of a semiconductor with adsorbed atoms by Morgenstern et al. [9]. I have used the method devised by Chhabra and Jensen [68] to determine the $f(\alpha)$ spectrum.

For any given box length L, one divides the system into square boxes, where one can calculate a *probability* $P_i(L)$ for every box i by adding up the numerical values of all pixels contained in the box. These must be normalised, so the sum over all boxes $\sum_i P_i(L) = 1$ for any L. Each of these boxes is given a *measure* $\mu_i(q, L)$ which depends on the moment q, given by $\mu_i(q, L) = [P_i(L)]^q / \sum_i [P_i(L)]^q$, again normalised. Applying this distortion leads to a new dimension $f(q)$ given by

$$f(q) = \lim_{L \to 0} \frac{\sum_i \mu_i(q, L) \log \mu_i(q, L)}{\log L}, \tag{4.1}$$

as well as a *singularity strength* $\alpha(q)$ given by

$$\alpha(q) = \lim_{L \to 0} \frac{\sum_i \mu_i(q, L) \log P_i(q, L)}{\log L}. \tag{4.2}$$

One can easily determine the multifractal dimension using

$$D_q = \frac{q\alpha(q) - f(q)}{q - 1}. \tag{4.3}$$

For the normal box counting procedure, I used the slope of $\log N$ versus $\log L$ to find the dimension. However to determine f, α or D_q at high or low values of q, this would not produce correct results because the data points for small box sizes would deviate. I think this is because of the limited precision used when solving the Schrödinger equation

numerically. As such, I have taken a range of box sizes for which the fraction in equation (4.1) does not show large deviations and averaged over those box sizes instead of taking a limit. This method is sufficiently accurate to determine whether an object is a monofractal or a multifractal.

What I will use in this chapter is the $f(\alpha)$ spectrum generated by calculating $f(q)$ and $\alpha(q)$ for various values of q and plotting them against each other. In the next section, I will show how this spectrum can be used to determine whether a fractal is a monofractal or multifractal.

4.1 Results for fractals

As a reference, I have calculated the $f(\alpha)$ spectrum of the Koch curve, a known monofractal, and the Hénon attractor, a known multifractal. I will use these in the next section to interpret the spectrum of electronic states in the Sierpiński triangle.

Monofractal: Koch curve
I have calculated the $f(\alpha)$ spectrum for the Koch curve of figure 3.1, which can be found in figure 4.3. The number of boxes ranges from 50×50 to 150×150. For positive values of q, f decreases somewhat, with hardly any change in α; this is probably a numerical artifact coming from the low resolution of the figure. For negative values, $f(\alpha)$ becomes parabolic. This is unlike a multifractal for which the entire spectrum, for positive and negative q, is expected to be parabolic [69].

Multifractal: Hénon attractor
Next, I have calculated the $f(\alpha)$ spectrum for the Hénon attractor, which can be found in figure 4.4. The number of boxes ranges from 50×50 to 150×150. It more or less resembles a parabola, which is as expected for a multifractal [69]. From this image, one can conclude that the Hénon attractor contains components of different length scales α that show different fractal behaviour.

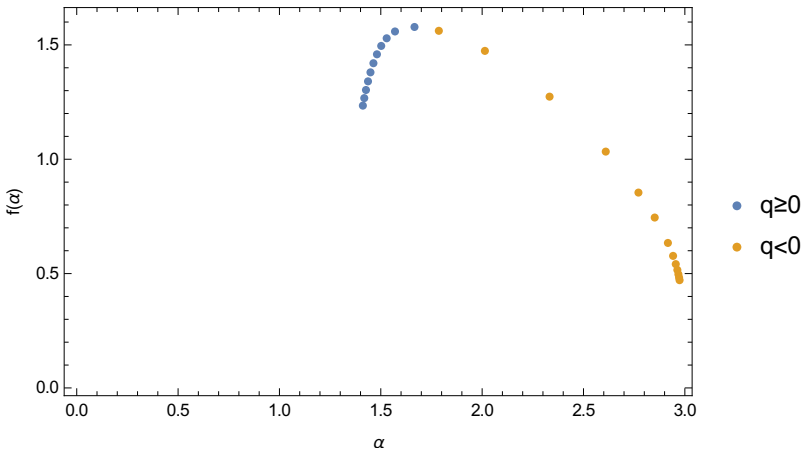

Figure 4.3: $f(\alpha)$ for the Koch curve shown in figure 3.1. The values of q used range from -5 to $+5$ in steps of 0.5, with additional data points for -0.25, -0.75, and -1.25.

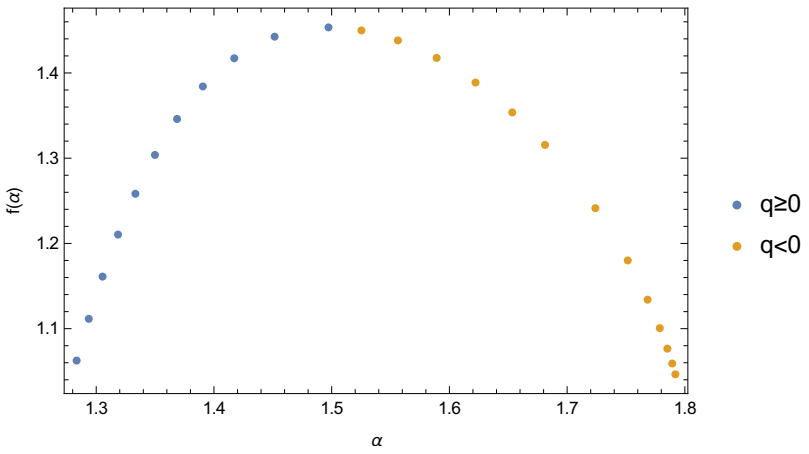

Figure 4.4: $f(\alpha)$ for the Hénon attractor shown in figure 4.1. The values of q used range from -5 to $+5$ in steps of 0.5, with additional data points for -0.25, -0.75, and -1.25.

4.2 Results for electronic states in fractals

Finally, I have calculated the $f(\alpha)$ spectrum for the wave functions at various energy levels of the Sierpiński triangle. The number of boxes ranges from 150×150 to 500×500. The results can be found in figure 4.5.

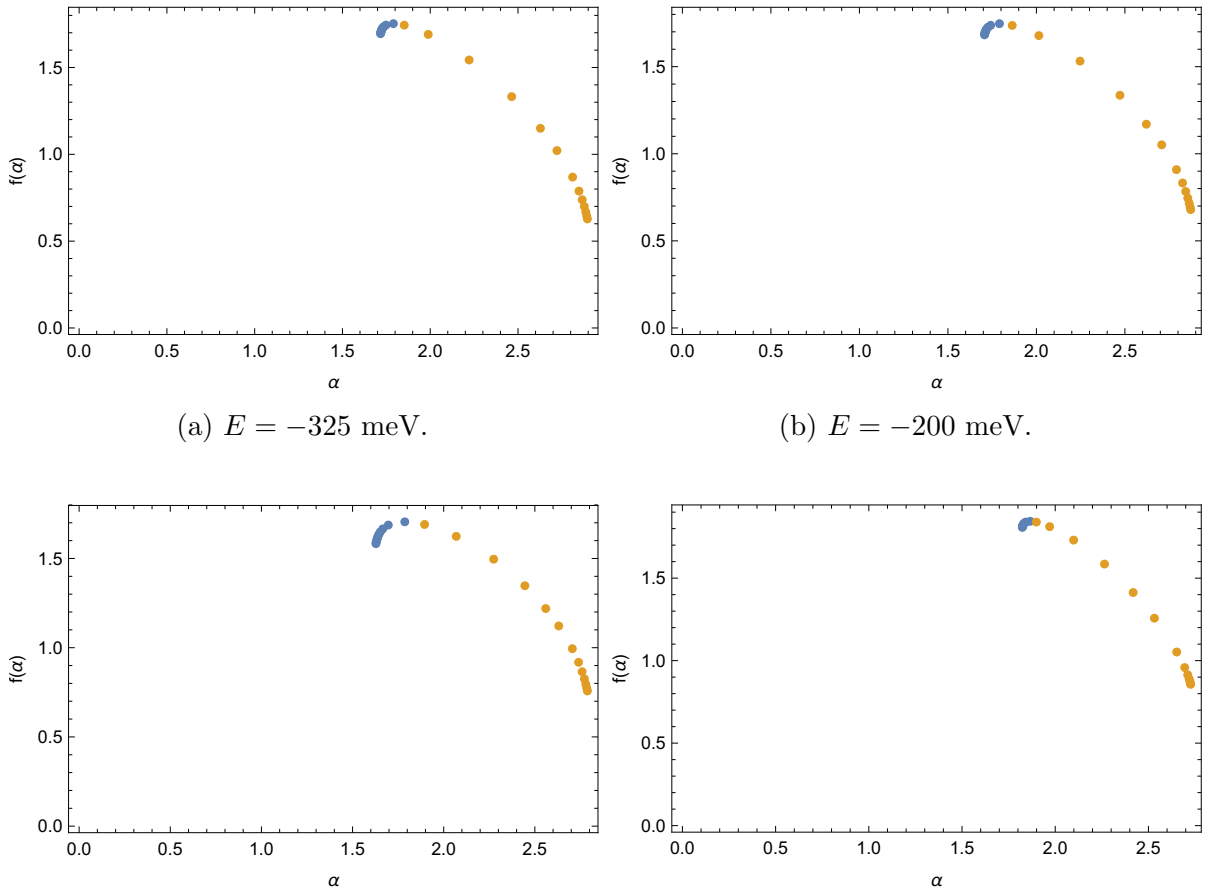

(a) $E = -325$ meV.

(b) $E = -200$ meV.

(c) $E = -100$ meV.

(d) $E = +100$ meV.

Figure 4.5: $f(\alpha)$ for the muffin-tin wave function maps shown in figure 3.5 at the same four energies. The data points for $q < 0$ are plotted in yellow, those for $q \geq 0$ in blue. The values of q used range from -5 to $+5$ in steps of 0.5, with additional data points for 0.25, 0.75, and 1.25.

Comparing these results with the known spectrum of a monofractal (figure 4.3) and a multifractal (figure 4.4), one can see that the spectrum closely resembles that of a monofractal. One concludes that the wave functions of electrons confined to this monofractal are themselves good approximations of monofractals.

Chapter 5

Three-dimensional topological insulators

The previous chapter described the surface states of copper, which are electrons that can be described by the Schrödinger equation as they have a nonzero effective mass. Spin does not play an important role in the problems described in the previous chapter, apart from introducing a twofold degeneracy. The surface states in graphene [70] and 3D topological insulators [11], however, can be described as massless Dirac fermions. Massless means that the dispersion relation (energy as a function of momentum) is linear instead of quadratic. Furthermore it is important to consider spin when considering Dirac fermions, as I will show later. Patterned graphene has already been widely studied theoretically [12–15, 71–74] and in experiments focusing on applications in electronics and energy storage [75–77]. Patterning 3D topological insulators however is relatively new. I will start with a theoretical study of the different kinds of potentials possible for 3D topological insulators, and compare them to the results known for graphene. These potentials represent different kinds of nanoparticles that could be placed on the surface of a 3D topological insulator. In this chapter, I will use TI to denote a 3D topological insulator.

The surface states of TIs are massless spin-$\frac{1}{2}$ fermions, described by the following low-energy effective Hamiltonian:

$$H = v_F(\vec{\sigma} \times \vec{p}) \cdot \hat{z} = v_F(\sigma_x \hat{p}_y - \sigma_y \hat{p}_x) \tag{5.1a}$$

$$= v_F \begin{pmatrix} 0 & \hat{p}_y + i\hat{p}_x \\ \hat{p}_y - i\hat{p}_x & 0 \end{pmatrix}, \tag{5.1b}$$

where v_F is the Fermi velocity and $\vec{\sigma}$ the vector formed by the three Pauli matrices [10]. As I am working with spin-$\frac{1}{2}$ particles, states to which this operator is applied are two-component spinors. This Hamiltonian differs from the one for graphene [15] given by

$$H = v_F \vec{\sigma} \cdot \vec{p} = v_F(\sigma_x p_x + \sigma_y p_y), \tag{5.2}$$

by replacing the dot product with a cross product.

At first sight, the introduction of a cross product in the Hamiltonian of equation (5.1) just causes a rotation in spin space given by $x \to y$ and $y \to -x$. However, in a TI, $\vec{\sigma}$ represents real spin, while in graphene it represents pseudospin and the real spin is not coupled to momentum. As a result, the surface states of a TI are *helical*, or, in other words, feature

spin-momentum locking. This difference becomes relevant when introducing magnetic fields, because there are two different ways in which a magnetic field can act on the surface states.

Magnetic fields act on electric charges via the Lorentz force, which can be described using a vector potential shifting the momentum of the particles (minimal coupling), but electrons also carry a magnetic moment of themselves which features Zeeman interaction with a magnetic field. The Zeeman interaction is proportional to the field $\vec{B}$ rather than the potential $\vec{A}$, which means that it falls off faster with distance. This makes it a prominent effect at short distances, such as a magnetised nanoparticle placed on top of a TI surface [46]. The Zeeman interaction splits the real spin states in graphene, while the Lorentz interaction splits the pseudospin states. This introduces a difference between (real) spin of a TI and pseudospin of graphene, which is more than just a rotation in spin space.

For an analysis of the Lorentz interaction, which is similar in graphene, I will refer to the literature [71, 72]. In this chapter, I will analyse the Zeeman interaction in way comparable to the treatment of interactions with graphene's pseudospin. The starting point is the plane wave solution to the Hamiltonian of equation (5.1) given by

$$\Psi_{\vec{k}}(\vec{x}) = Ae^{i\vec{k}\cdot\vec{x}} \begin{pmatrix} i \\ e^{i\phi} \end{pmatrix}, \tag{5.3}$$

with ϕ the polar angle of the wave vector $\vec{k}$. The $\hat{p}_i$ operators are defined as $-i\hbar\frac{\partial}{\partial x_i}$ which means their eigenvalues are given by $\hbar v_F k_i$ and represent the components of the plane wave's momentum. The related polar angle ϕ however, determines the spinor, and that is how we get spin-momentum locking.

To become acquainted with the behaviour of Dirac fermions, I will first present a study of a *quasi-1D* system with a barrier of finite width, which extends in the y-direction. I will use the wave function of equation (5.3) to describe scattering against such a barrier. To do so, I will assume a rightwards incoming particle. I will define $\phi = \arctan(k_y/k_x)$ in the interval $-\pi/2 < \phi < \pi/2$, $k = |\vec{k}|$, and $p = \hbar k$. Here, ϕ is then the incident angle of the particle, and the angle of reflection is given by $\pi - \phi$. The reflected particle is obtained by transforming $k_x \to -k_x$ and $\phi \to \pi - \phi$:

$$\Psi(x,y) = Ae^{ip(x\cos\phi + y\sin\phi)/\hbar} \begin{pmatrix} i \\ e^{i\phi} \end{pmatrix} + re^{ip(-x\cos\phi + y\sin\phi)/\hbar} \begin{pmatrix} i \\ e^{i(\pi-\phi)} \end{pmatrix} \tag{5.4a}$$

$$= Ae^{i(k_x x + k_y y)} \begin{pmatrix} i \\ (k_x + ik_y)/k \end{pmatrix} + re^{i(-k_x x + k_y y)} \begin{pmatrix} i \\ (-k_x + ik_y)/k \end{pmatrix}. \tag{5.4b}$$

with A and r the amplitudes of the incoming and reflected wave function, respectively. It should be noted that the spinor changes under reflection, which means that any scattering process needs to change spin. When using $\phi = 0$, the equation essentially describes a 1D system as the dependence on y drops out. In this 1D case, the incident and reflected state are orthogonal eigenstates of the Hamiltonian, and as such not coupled to each other. Scattering at $\phi = 0$ thus requires a perturbation which couples the two states.

I will consider two different potentials to add to this system: the electrostatic potential $V(\vec{r})$ for comparison with graphene literature and the magnetic field $\vec{B}(\vec{r})$ via the Zeeman

interaction. The Hamiltonian with both potentials included reads

$$H = v_F(\vec{\sigma} \times \vec{p}) \cdot \hat{z} + V(\vec{r})\mathbb{I} - \vec{m} \cdot \vec{B}(\vec{r}) \tag{5.5a}$$

$$= \begin{pmatrix} V + mB_z & (v_F\hat{p}_y + mB_x) + i(v_F\hat{p}_x - mB_y) \\ (v_F\hat{p}_y + mB_x) - i(v_F\hat{p}_x - mB_y) & V - mB_z \end{pmatrix}, \tag{5.5b}$$

using the magnetic moment of the electron $\vec{m} = -m\vec{\sigma}$, with $m = g_s\mu_B$ with g_s the effective gyroscopic factor and μ_B the Bohr magneton. As an example, the Zeeman gyroscopic factor was found to be 23 ± 3 out-of-plane and 32 ± 3 in-plane for surface states of Bi_2Se_3 [78], but close to 2 for Bi_2Te_2Se [79].

An electrostatic barrier shifts the energies but does not couple to spin. This has interesting consequences: electrostatic barriers are transparent to massless Dirac fermions incident at $\phi = 0$ (or in any one-dimensional problem). This also applies to massive particles if the mass times v_F^2 is negligible compared to the potential V. As wave functions described by the Schrödinger equation show exponential decay inside a barrier, this was an unexpected result. It is known as the *Klein paradox* [12]. A magnetic field in the z-direction on the other hand, produces a term similar to the mass term in the Hamiltonian of a massive Dirac particle [13]. This couples the spin states as σ_z does not commute with the kinetic part of the Hamiltonian.

In the next section, I will first introduce the transfer matrix method to study a quasi-1D system. Next, I will use this method to show that there is indeed Klein tunnelling through electrostatic barriers, but a gap opens for z-magnetic barriers analogous to a massive Dirac particle.

5.1 Transfer matrix method for single barriers

I will assume a square potential that extends from $x = x_1$ to $x = x_2$ and infinitely in the y-direction. The wave function in that case is divided into three regions, ψ_1 left of the barrier, ψ_2 inside the barrier and ψ_3 right of the barrier. In the ψ_2 region, a potential is applied. The boundary conditions between these regions are given by

$$\psi_1(x_1, y) = \psi_2(x_1, y), \tag{5.6a}$$

$$\psi_2(x_2, y) = \psi_3(x_2, y). \tag{5.6b}$$

The three regions of the wave function and the incident angle ϕ can be seen in figure 5.1. I will set the amplitude of the incoming wave to 1 and will assume there is no incoming wave from the right. ψ_1 and ψ_3 can then be defined as

$$\psi_1(x, y) = e^{ip(x\cos\phi + y\sin\phi)/\hbar}\begin{pmatrix} i \\ e^{i\phi} \end{pmatrix} + re^{ip(-x\cos\phi + y\sin\phi)/\hbar}\begin{pmatrix} i \\ e^{i(\pi-\phi)} \end{pmatrix}, \tag{5.7a}$$

$$\psi_3(x, y) = te^{ip(x\cos\phi + y\sin\phi)/\hbar}\begin{pmatrix} i \\ e^{i\phi} \end{pmatrix}, \tag{5.7b}$$

with t the transmission amplitude and r the reflection amplitude. The definition of ψ_2 depends on the type of potential applied. In any case, the conserved quantities in the problem are the energy $v_F p$ and the y-momentum $p\sin\phi$, as equations (5.6) should hold

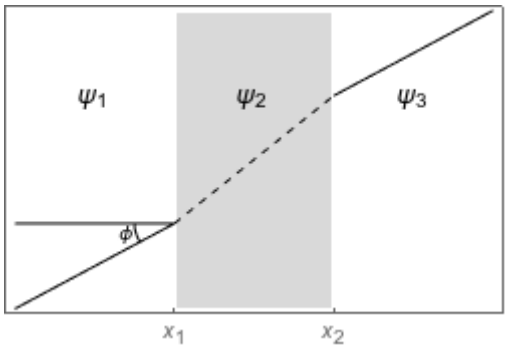

Figure 5.1: A particle incident at angle ϕ being transmitted through a quasi-1D barrier, showing the three regions of the wave function ψ.

regardless of the value of y. I will first discuss the transfer matrix method used to solve these equations and then I will discuss a number of different potentials.

I will use the method described by McKellar and Stephenson Jr. [80] to calculate the scattering matrix of this system. To do so, the wave functions ψ_1, ψ_2, and ψ_3 have to be arranged in a matrix form, by separating the forwards and backwards components and the two components of the spinor. For a wave function of the form

$$\psi(x,y) = a_1 \begin{pmatrix} \psi_{\uparrow,A}(x) \\ \psi_{\downarrow,A}(x) \end{pmatrix} + a_2 \begin{pmatrix} \psi_{\uparrow,B}(x) \\ \psi_{\downarrow,B}(x) \end{pmatrix} \tag{5.8}$$

with a_1 and a_2 the amplitudes of the forwards and backwards components A and B, the Ω matrix can be written as

$$\Omega(x) = \begin{pmatrix} \psi_{\uparrow,A}(x) & \psi_{\uparrow,B}(x) \\ \psi_{\downarrow,A}(x) & \psi_{\downarrow,B}(x) \end{pmatrix}. \tag{5.9}$$

The plane waves on either side of the barrier can then be connected to each other using the *matching matrix*

$$M = \Omega_3^{-1}(x_2)\Omega_2(x_2)\Omega_2^{-1}(x_1)\Omega_1(x_1), \tag{5.10}$$

with Ω_1, Ω_2, and Ω_3 being the matrices constructed from ψ_1, ψ_2, and ψ_3, respectively, using the method described above. For this purpose, ψ_3 has been given a backwards component, similar to the one in ψ_1, even though in a physical scattering process, with a particle incoming from the left, the amplitude of this component will be zero. With ψ_1 as given by equation (5.8), the amplitudes b_1 and b_2 of the two components of ψ_3 are then given as

$$\begin{pmatrix} b_1 \\ b_2 \end{pmatrix} = M \begin{pmatrix} a_1 \\ a_2 \end{pmatrix}. \tag{5.11}$$

Another way to treat this problem is by using a scattering matrix, defined as

$$S = \begin{pmatrix} t & r' \\ r & t' \end{pmatrix} \Leftrightarrow \begin{pmatrix} b_1 \\ a_2 \end{pmatrix} = S \begin{pmatrix} a_1 \\ b_2 \end{pmatrix}, \tag{5.12}$$

with t' and r' the transmsision and reflection amplitudes of a wave coming from the right. From equation (5.11), we find that

$$b_1 = M_{11}a_1 + M_{12}a_2, \tag{5.13a}$$
$$b_2 = M_{21}a_1 + M_{22}a_2, \tag{5.13b}$$

and from equation (5.12), we find that

$$b_1 = S_{11}a_1 + S_{12}b_2, \tag{5.14a}$$
$$a_2 = S_{21}a_1 + S_{22}b_2. \tag{5.14b}$$

Equation (5.13b) can be rewritten to

$$a_2 = \frac{b_2 - M_{21}a_1}{M_{22}}. \tag{5.15}$$

Combining this with equation (5.13a), we find

$$b_1 = \left(M_{11} - \frac{M_{12}M_{21}}{M_{22}}\right) a_1 + \frac{M_{12}}{M_{22}} b_2. \tag{5.16}$$

Equating these two results to equations (5.14a) and (5.14b), we find the components of the S-matrix, given by

$$S_{11} = \left(M_{11} - \frac{M_{12}M_{21}}{M_{22}}\right), \tag{5.17a}$$
$$S_{12} = \frac{M_{12}}{M_{22}}, \tag{5.17b}$$
$$S_{21} = \frac{-M_{21}}{M_{22}}, \tag{5.17c}$$
$$S_{22} = \frac{1}{M_{22}}. \tag{5.17d}$$

Using $\det M = M_{11}M_{22} - M_{12}M_{21}$, we can now write down the S-matrix as

$$S = \frac{1}{M_{22}} \begin{pmatrix} \det M & M_{12} \\ -M_{21} & 1 \end{pmatrix}. \tag{5.18}$$

The transmission and reflection coefficients can now be calculated as $T = |t|^2$ and $R = |r|^2$.

I will use this method to describe transmission through a single barrier using different kinds of potentials, applying an electrostatic potential in every case, which gives the energy scale.

5.1.1 Electrostatic potential

When only considering an electrostatic barrier with a fixed height $V(\vec{r}) = V$ inside the barrier and $V(\vec{r}) = 0$ outside, the Hamiltonian (5.5) inside the barrier becomes

$$H = \begin{pmatrix} V & v_F(\hat{p}_y + i\hat{p}_x) \\ v_F(\hat{p}_y - i\hat{p}_x) & V \end{pmatrix}. \tag{5.19}$$

Its eigenvalues as a function of wave vector (k_x, k_y) are given by

$$E = V \pm \hbar v_F \sqrt{k_x^2 + k_y^2}, \tag{5.20}$$

and outside the barrier, the energy of a particle is given by

$$E = v_F p. \tag{5.21}$$

Using conservation of energy and of k_y, we can find a new value of k_x in terms of V and the properties of the incoming wave p and ϕ:

$$\hbar k'_x = \pm\sqrt{(p - V/v_F)^2 - (p\sin\phi)^2}. \tag{5.22}$$

Again, there are two states, a forward and a reflected one, unless k'_x is imaginary: an imaginary k'_x will lead to a state which decays exponentially and one which increases exponentially.

This k'_x can be inserted in place of the k_x in equation (5.4b) to find the wave function ψ_2 inside the barrier, given by

$$\psi_2(x,y) = a_1 e^{i(k'_x x + k_y y)} \begin{pmatrix} i \\ k'_x + ik_y \end{pmatrix} + a_2 e^{i(-k'_x x + k_y y)} \begin{pmatrix} i \\ -k'_x + ik_y \end{pmatrix}. \tag{5.23}$$

For $\phi \neq 0$, this change of angle causes a coupling between leftwards and rightwards states because the spinors in region 2 have a complex phase different from the one in region 1 and 3. It therefore becomes possible to scatter off the barrier and part of the wave function will be reflected. When $|\sin\phi| > |v_F p - V|/v_F p$, k'_x becomes imaginary and in this case it is also possible for the wave function to reflect *inside* the barrier, leading to resonances.

As an example of this resonance phenomenon, I have numerically determined the scattering matrix S for various values of $v_F p$ below the potential barrier V. The width of the barrier is set to $12\hbar v_F/V$. The resulting transmission probability as a function of the incident angle for a number of different momenta can be seen in figure 5.2.

I indeed observe *Klein tunnelling* at $\phi = 0$ at any of these momenta, as expected because scattering is not possible at this angle. Interestingly, the case $p = 0.2V/v_F$ shows a large transmission over a wide angle, while $p = 0.5V/v_F$ shows narrow peaks in the transmission probability caused by resonances inside the barrier. The $p > V$ case shows resonances spaced more closely together, increasing with momentum. The results show some similarities to graphene for $p < V/v_F$ [12] and $p > V/v_F$ [13], which also show resonances in the former case and an angle of transmission increasing with energy in the latter case.

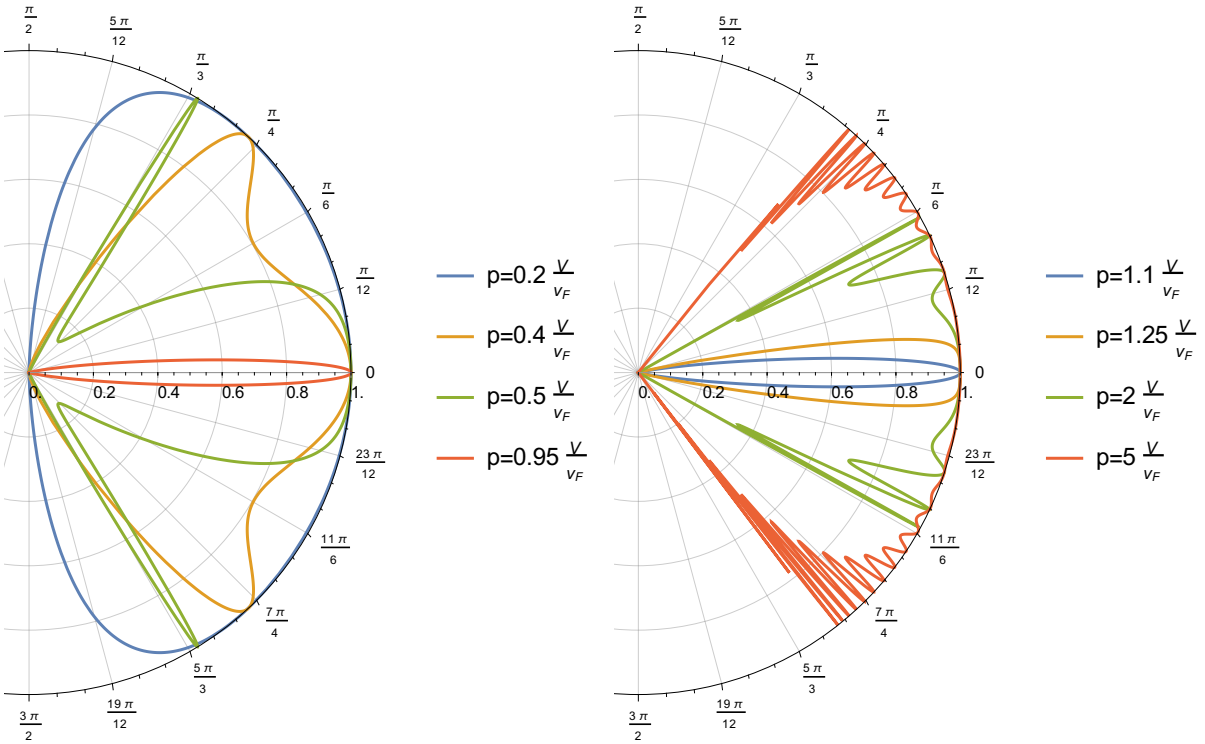

(a) $p < V/v_F$ (b) $p > V/v_F$

Figure 5.2: The transmission probability as a function of the incident angle in a system with an electrostatic potential barrier, for different incoming momenta p greater or smaller than V/v_F.

5.1.2 Out-of-plane magnetic field

When only an electrostatic potential and a z-magnetic field are considered, the Hamiltonian (5.5) inside the barrier becomes

$$H = \begin{pmatrix} V + mB_z & v_F(\hat{p}_y + i\hat{p}_x) \\ v_F(\hat{p}_y - i\hat{p}_x) & V - mB_z \end{pmatrix}. \tag{5.24}$$

The $mB_z\sigma_z$ term added is similar to the mass term in the Dirac equation for massive fermions. Applying this potential is thus equivalent to making the particle massive instead of massless in a certain region, which is theoretically possible in graphene too.

Its eigenvalues are given by

$$E = V \pm \sqrt{\hbar^2 v_F^2 (k_x'^2 + k_y^2) + m^2 B_z^2}, \tag{5.25}$$

and conservation of energy and y-momentum leads to

$$\hbar v_F k_x' = \pm\sqrt{(v_F p - V)^2 - (v_F p \sin\phi)^2 - m^2 B_z^2}, \tag{5.26}$$

which can be inserted into equation (5.23). The result of this mass is thus that k_x' turns imaginary for any angle when the incoming momentum is in the "gap" $V - mB_z < v_F p < V + mB_z$, and Klein tunnelling in this gap is suppressed.

I have repeated the same numerical calculations for a mass of $mB_z = 0.1V$. This means there is a gap at $0.9V/v_F < p < 1.1V/v_F$. As expected, inside the gap Klein tunnelling almost disappears, and on either side of the gap resonances are observed similar to those in the purely electrostatic case. This is similar to results for mass barriers in graphene [13, 15], and in line with existing calculations for surface resistance of TIs, which indicate that a z-magnetic field can cause a large electrical resistance depending on the Fermi level [16]. Experimentally, such a gap was found in Bi_2Se_3 doped with Mn [81]. However Fe atoms adsorbed on Bi_2Se_3 were found to align there magnetic moment in-plane, opening no gap [46, 47]. I will discuss in-plane magnetic fields in the next section.

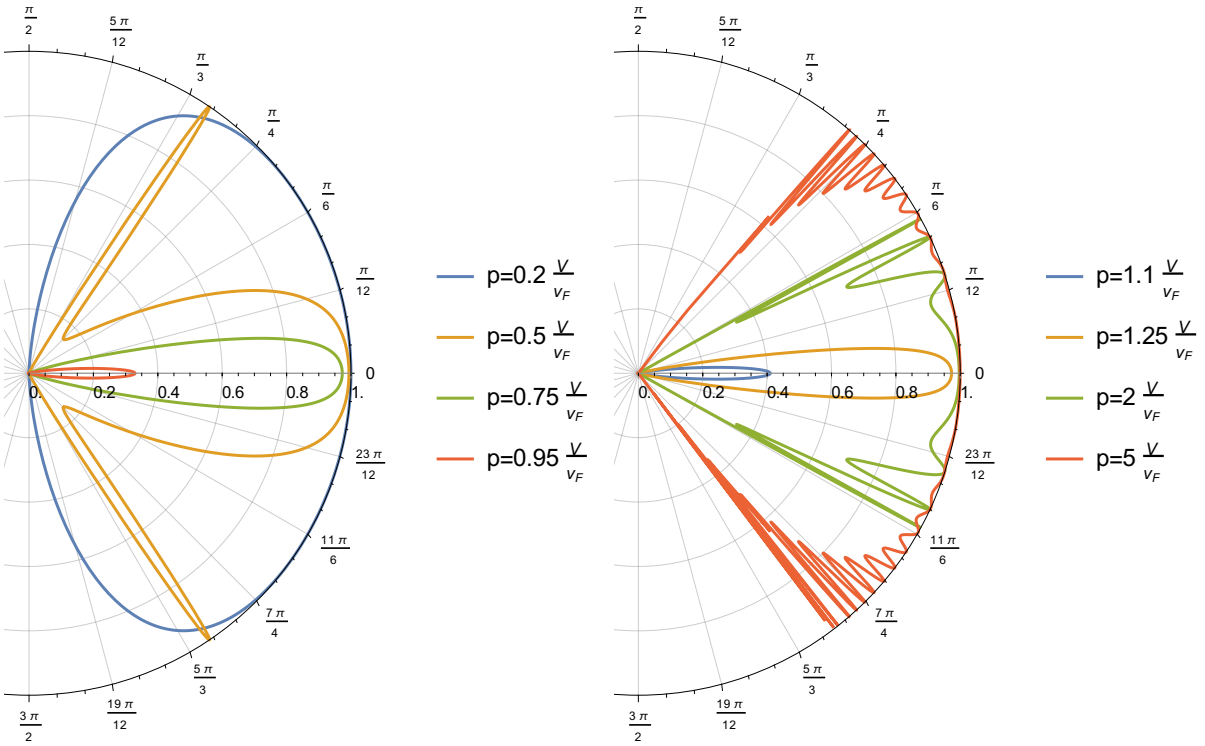

(a) $p < V/v_F$ (b) $p > V/v_F$

Figure 5.3: The transmission probability as a function of the incident angle in a system with an electrostatic and $z$magnetic potential barrier, for different incoming momenta p greater or smaller than V/v_F and a magnetic field $mB_z = 0.1V/v_F^2$.

5.1.3 In-plane magnetic field

While applying a magnetic field out-of-plane in the z-direction induces a mass, applying a magnetic field in-plane in the x- or y-direction shifts the momentum. When V, mB_x and mB_y are included, the Hamiltonian (5.5) becomes

$$H = \begin{pmatrix} V & (v_F\hat{p}_y + mB_x) + i(v_F\hat{p}_x - mB_y) \\ (v_F\hat{p}_y + mB_x) - i(v_F\hat{p}_x - mB_y) & V \end{pmatrix}, \tag{5.27}$$

with B_x and B_y the magnetic field in the x- and y-direction, respectively. Note that B_x shifts $\hat{p}_y$ and the other way around with a sign difference, because the momentum has a cross product with spin in the Hamiltonian and the magnetic field a dot product.

The eigenvalues of this Hamiltonian are given by

$$E = V \pm \sqrt{(\hbar v_F k_x - mB_y)^2 + (\hbar v_F k_y + mB_x)^2}, \tag{5.28}$$

and conservation of energy and y-momentum then leads to a new x-momentum of the plane wave given by

$$\hbar v_F k'_x = mB_y \pm \sqrt{(v_F p - V)^2 - (mB_x + v_F p \sin\phi)^2}. \tag{5.29}$$

The eigenfunctions of this Hamiltonian are given by

$$\begin{aligned}\psi_2(x,y) = a_1 e^{i(k'_x x + k_y y)} &\begin{pmatrix} i \\ (k'_x - mB_y/\hbar v_F) + i(k_y + mB_x/\hbar v_F) \end{pmatrix} \\ + a_2 e^{i(-k'_x x + k_y y)} &\begin{pmatrix} i \\ -(k'_x - mB_y/\hbar v_F) + i(k_y + mB_x/\hbar v_F) \end{pmatrix}.\end{aligned} \tag{5.30}$$

We can see here that B_x shifts the y-momentum in the spinor but not that of the plane wave (which is conserved by the translational symmetry of the potential). This means that the angle under which Klein tunnelling happens is shifted away from zero. As k'_x changes, the energies of states are shifted too. For large fields it is possible for k'_x to become imaginary, causing the wave function to fall off exponentially like it did for out-of-plane magnetic fields.

A y-magnetic field on the other hand leaves the spinor invariant but changes the shape of the plane wave. This merely introduces a complex phase to the matching matrix M which does not change the probability of transmission or reflection.

In figure 5.4 numerical results can be seen for $B_x = 0.1V/v_F m$. One can see here that the angle of Klein tunnelling is now nonzero as expected. As k'_x is shifted in different directions for positive and negative ϕ, the energies of resonances caused by reflections inside the barrier do so too. This can be seen in the plot for the resonance near $\phi = \pm\pi/3$: it appears at $p = 0.5V/v_F$ in figure 5.2, and at $p = 0.45V/v_F$ and $p = 0.55V/v_F$ for positive and negative ϕ, respectively, in figure 5.4.

I will give a further interpretation of this in section 5.2.4 when discussing the band structure of 2D systems with an in-plane magnetic field.

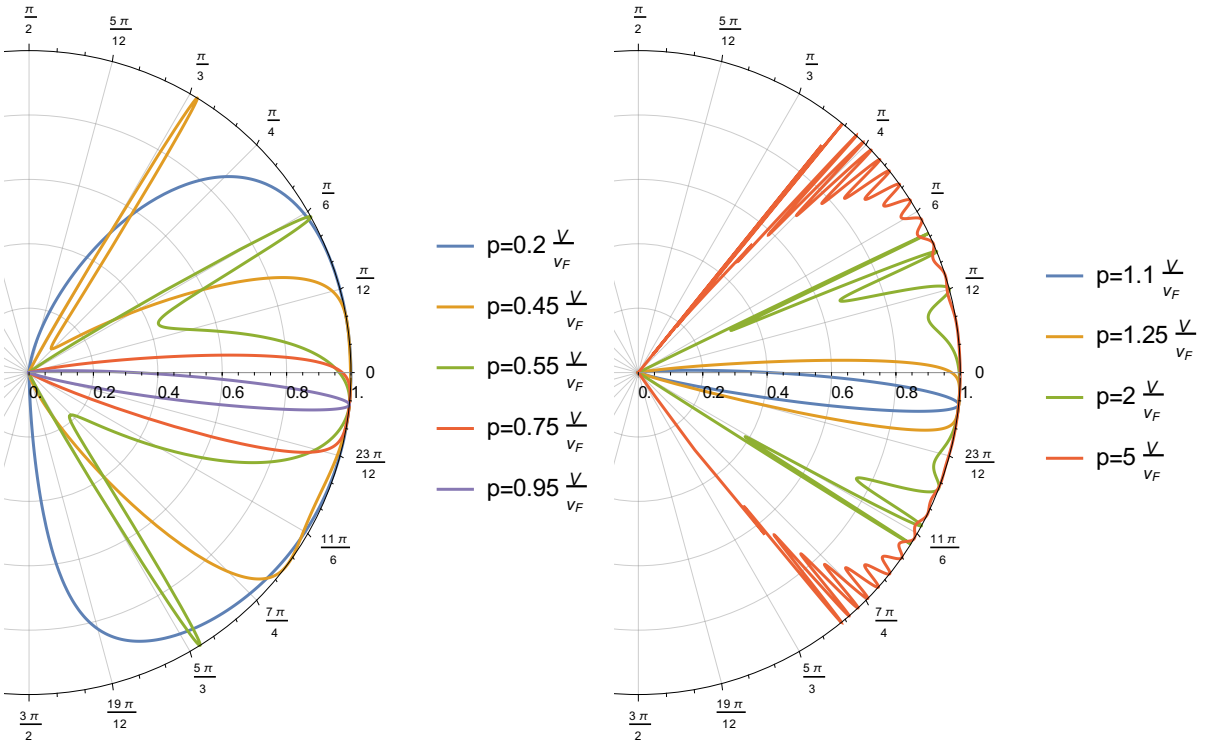

(a) $p < V/v_F$ (b) $p > V/v_F$

Figure 5.4: The transmission probability as a function of the incident angle in a system with an electrostatic and x-magnetic potential barrier, for different incoming momenta p greater or smaller than the height of the barrier and a magnetic field $B_x = 0.1V/v_F m$.

5.1.4 Delta barrier

For a 1D system (a wave with incident angle $\phi = 0$) the transmission coefficient through an electrostatic barrier in a one-dimensional system is given by McKellar and Stephenson Jr. [82] as

$$T = \frac{1}{1 + \frac{1}{4}\left(\frac{\Lambda}{\lambda} - \frac{\lambda}{\Lambda}\right)^2 \sin^2(Ka)}, \tag{5.31}$$

with $\lambda = \frac{\hbar v_F k}{E + m v_F^2}$, $\Lambda = \frac{\hbar v_F K}{E - V + m v_F^2}$, $\hbar v_F K = \sqrt{(E-V)^2 - m^2 v_F^4}$, where m is the mass of the particle, V the height, and a the width of the barrier. The period of this oscillation is found by setting $Ka = n\pi$ with $n \in \mathbb{Z}$. When $k \ll V$ and $m \ll V$, this condition simplifies to a condition for the area A of the barrier which is $A = Va = n\pi\hbar v_F$, indicating that Klein tunnelling is possible for particles of a small mass if the area of a delta barrier is a multiple of $\pi\hbar v_F$.

Setting $m = 0$, one finds $\left(\frac{\Lambda}{\lambda} - \frac{\lambda}{\Lambda}\right) = 1$ which results in Klein tunnelling for all kinds of electrostatic barriers at $\phi = 0$, just as observed in section 5.1.1. However, in the previous sections we already found that Klein tunnelling does not occur at greater angles. As such, I will now study the massless system numerically at a finite angle, approximating an electrostatic delta peak using a potential of height $10^3\ \hbar v_F k$ and width between 0 and $10^{-2}\ \hbar v_F / V$, to find out what happens to Klein tunnelling at angles away from zero in

the case of a delta barrier.

In figure 5.5, a plot of the angular dependence of the transmission can be seen for a number of different areas of the delta barrier. In this plot, the transmission still appears to decrease with the area of the barrier; however, the transmission as a function of area for a fixed angle in figure 5.6 indicates that the transmission is cyclic.

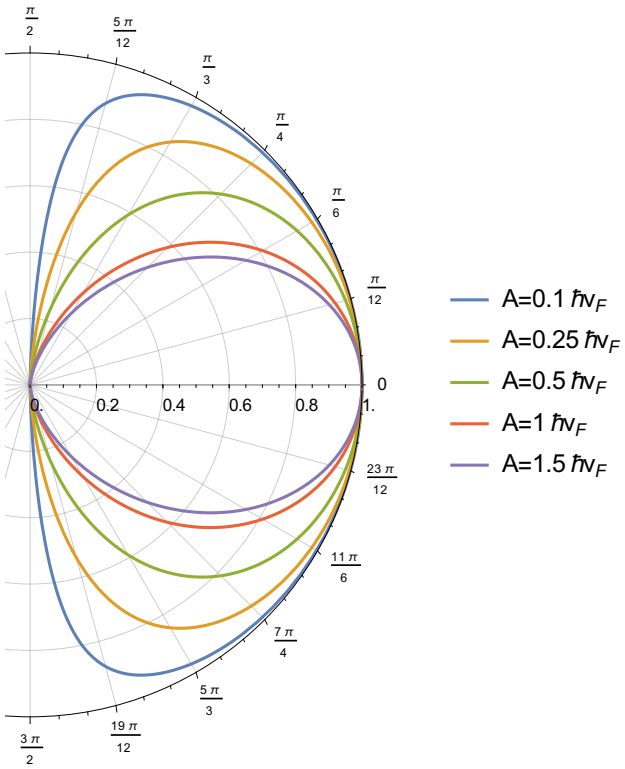

Figure 5.5: The transmission probability as a function of the incident angle in a system with an electrostatic delta barrier, for different areas of the barrier.

Interestingly, the period of this cyclic phenomenon is very close to the value of π found in a 1D system with a (slightly) massive particle. These results are similar to results found for graphene [14], which also show Klein tunnelling around $\phi = 0$ and cyclic transmission at greater angles.

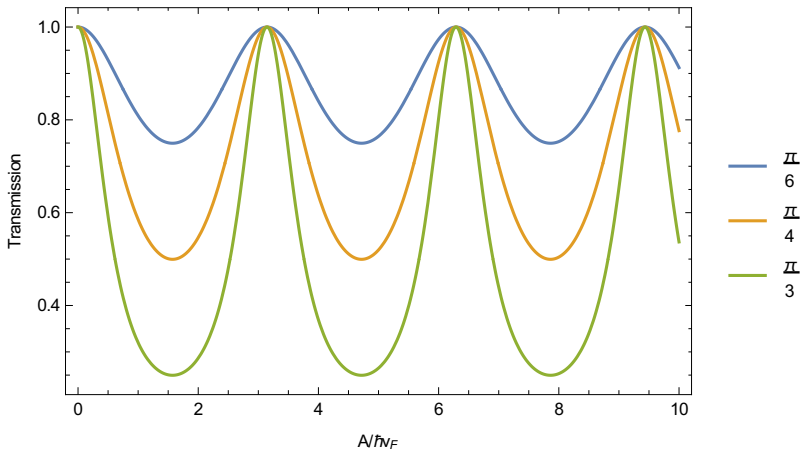

Figure 5.6: The transmission probability as a function of the area of the barrier in a system with an electrostatic delta barrier, at a number of angles ϕ. The period of oscillation is approximately 3.14.

As expected from section 5.1.2, a mass barrier (in a TI equivalent to a z-magnetic field interacting with the electron magnetic moment) kills Klein tunnelling. While the results for finite barriers still showed an enlarged transmission around $\phi = 0$, the result for a mass barrier in the delta limit does not depend on the angle anymore. The cyclic phenomenon from an electrostatic delta peak is also not observed; transmission decreases with the area of the barrier, as can be seen in figure 5.7.

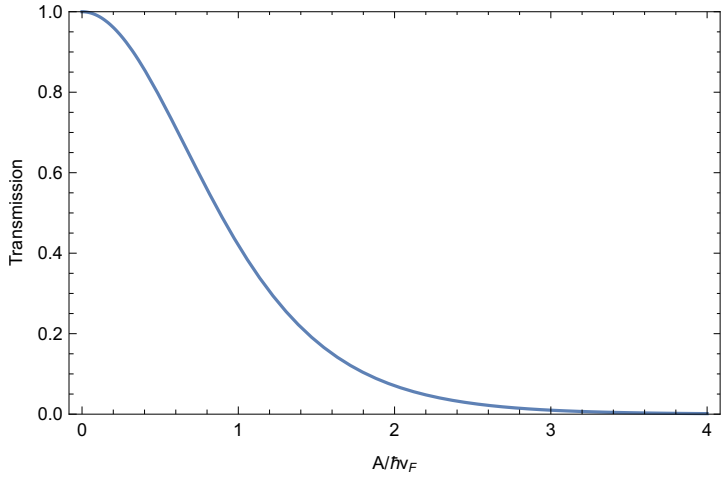

Figure 5.7: The transmission probability as a function of the area of the barrier in a system with a z-magnetic delta barrier. This does not depend on the incident angle. I have limited the width of the barrier to $4 \times 10^{-3}\ \hbar v_F/V$ in the plot, as transmission is already negligible for an area of $4\ \hbar v_F$.

I have repeated these calculations using a barrier with a fixed height of $10^4\ \hbar v_F k$ or one with a fixed width of $10^{-3}\ \hbar v_F/V$. In both cases, the resulting dependency on area is the same as in the plots above. This leads me to conclude that a potential barrier of height $10^3\ \hbar v_F k$ and width $< 10^{-2}$ is sufficiently narrow and peaked to study a delta barrier.

5.2 Multiple barriers and periodic systems

If multiple barriers are placed close to each other, so that the wave does not decohere travelling between the barriers, the transfer matrix method can be applied to a system of multiple barriers. This would imply multiplying the transfer matrices M of the barriers. However, I found that this procedure is not numerically stable. Instead, barriers can be combined by working with the scattering matrix directly [83, p. 126]. Two scattering matrices S_1 and S_2 whose values have the subscripts 1 and 2 can be combined as

$$S = \begin{pmatrix} 0 & r_1 \\ r_2' & 0 \end{pmatrix} + \frac{1}{1 - r_1' r_2} \begin{pmatrix} t_1 t_2 & r_1' t_2 t_2' \\ t_1 t_1' r_2 & t_1' t_2' \end{pmatrix}, \tag{5.32}$$

assuming the right side of system 1 connects to the left side of system 2. This procedure can be applied iteratively to describe any number of barriers. For a small number of barriers this is sufficient, but for a larger number one needs to use different methods. In the next section, I will explore band structures as a way of studying macroscopically large systems.

5.2.1 Band structure and the Bloch theorem

A single barrier or small number of barriers can be studied by calculating scattering probabilities directly. For larger systems this calculation becomes unfeasible. It is however possible to calculate the properties of a periodic system if one assumes that the system is so large that all finite-size effects are negligible. This means that we consider a system that is infinite, or at least macroscopically large. The assumption here is that the wave function of the system repeats itself after a (possibly macroscopic) number of unit cells N. This is known as the *Born–von Kármán* condition. From this condition, the Bloch theorem can be derived, which states that the energy states of electrons in a periodic potential can be described as

$$\psi(\vec{r}) = e^{i\vec{k}\cdot\vec{r}} u(\vec{r}), \tag{5.33}$$

with $u(\vec{r})$ a periodic function with the same periodicity as the system [53, pp. 135–139]. In the case of surface states of a TI, the functions $\psi(\vec{r})$ and $u(\vec{r})$ will be two-component spinors.

This means that a relation can be derived between the energy and *Bloch* or *crystal momentum* of a given state, which defines the band structure of the system. Note that the Bloch momentum is not the same as the incoming momentum of a particle before it hits a barrier; the momentum outside the barrier is instead directly related to the particle's energy. The Bloch momentum is not a real momentum of the electron; it is comparable to the group velocity of a wave packet, with the real momentum as phase velocity [84, p. 39].

In the quasi-1D systems considered here, the y-component of the momentum is conserved in the barriers. One can therefore take the Bloch k_y to be equal to the real k_y anywhere in the system. In the x-direction however the momentum differs inside and outside the barrier, and as such there is a distinct Bloch momentum describing the phase difference across one unit cell in a quasi-1D system. When treating quasi-1D systems, I will use k_x for the x-component of the incoming momentum and κ for the x-component of the Bloch

momentum. In 2D systems instead I will only work with Bloch $\vec{k}$ because the concept of incoming momentum is not defined there.

The quasi-1D potential that I use here is periodic with a unit cell of width l, containing one barrier of width $w < l$ extending infinitely in the y-direction. Two unit cells of the potential and their x-coordinates are shown in figure 5.8.

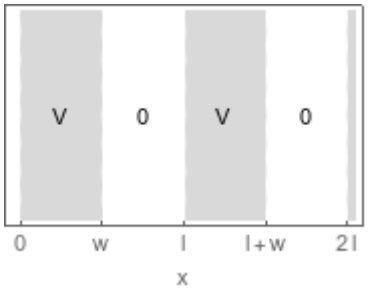

Figure 5.8: Two unit cells of length l of the quasi-1D periodic potential as a function of x showing the barriers of potential V with a width w.

To derive the properties of this periodic system, a matrix similar to the matching matrix of equation (5.10) is used. This *transfer matrix* is given by

$$T = \Omega_1(l)\Omega_1^{-1}(w)\Omega_2(w)\Omega_2^{-1}(0), \tag{5.34}$$

with Ω_1 describing the wave function outside the barrier and Ω_2 the one inside. The barriers are assumed to extend from $x = nl$ to $x = nl + w$ for $n \in \mathbb{Z}$. In the start of this section, we assumed that the wave function repeats itself after N unit cells, which means that $T^N = 1$. This means that the eigenvalues of the matrix are given by $e^{2\pi i n/N}$ and the trace is

$$\mathrm{Tr}(T) = 2\cos(2\pi i n/N). \tag{5.35}$$

One can now define the Bloch momentum as $\kappa = 2\pi n/L$ with $L = Nl$, or remove N and L from the equation by calculating it directly from the transfer matrix using [13, 80]

$$2\cos(\kappa l) = \mathrm{Tr}(T). \tag{5.36}$$

The matrix T here depends on k_y and the particle's energy. This equation sets up the relation between κ, k_y, and E necessary to calculate the band structure. For every value of $\mathrm{Tr}(T)$ in the interval $[-2, 2]$, there are two possible solutions in the first Brillouin zone $-\pi/l < \kappa < \pi/l$. A trace outside that interval indicates a band gap, where (in the limit of an infinite system) no states are allowed.

5.2.2 2D systems

Determining the band structure from the transfer matrix as done in the previous section, works well for 1D and quasi-1D systems. For two-dimensional potentials however, one cannot describe transmission of electrons in terms of the number of barriers passed. Instead, the bands can be described by reworking equation (5.33) into a matrix-vector equation by using the fact that the Fourier transform of a periodic function is discrete. I will derive this matrix-vector equation following Ashcroft and Mermin [53, pp. 137-138] replacing the kinetic term of the Schrödinger equation by equation (5.1).

The starting point for this derivation is again the Born–von Kármán condition, now in 2D, which tells us that the wave function repeats itself after a (possibly macroscopic) N_i amount of unit cells in the direction $i = x, y$. The Fourier transform of ψ is thus discrete and each spin component of it can be written as

$$\psi_\sigma(\vec{r}) = \sum_{\vec{q}} e^{i\vec{q}\cdot\vec{r}} c_{\vec{q},\sigma}, \tag{5.37}$$

with $\vec{q}$ a vector in reciprocal space and $\sigma = \pm 1$ associated with the up or down spin component. The vectors $\vec{q}$ need not be reciprocal lattice vectors as the periodicity of the wave function is larger than one unit cell.

For this wave function, the kinetic term given by equation (5.1) can be written as

$$v_F \begin{pmatrix} 0 & \hat{p}_y + i\hat{p}_x \\ \hat{p}_y - i\hat{p}_x & 0 \end{pmatrix} \cdot \psi(\vec{r}) = \hbar v_F \sum_{\vec{q}} e^{i\vec{q}\cdot\vec{r}} \begin{pmatrix} 0 & q_y + iq_x \\ q_y - iq_x & 0 \end{pmatrix} \cdot c_{\vec{q}} \tag{5.38a}$$

$$= \hbar v_F \sum_{\vec{q},\sigma} e^{i\vec{q}\cdot\vec{r}} (q_y + i\sigma q_x) c_{\vec{q},-\sigma}, \tag{5.38b}$$

where $c_{\vec{q}}$ is used to denote the vector containing both spin components $c_{\vec{q},\sigma}$.

As different potentials U act on the spinor in different ways, I will write it as a matrix $U_{\sigma\sigma'}$. An electrostatic potential is then given by a scalar potential times the identity matrix; a mass potential by a scalar times the Pauli matrix σ_z and the other two Pauli matrices describe an in-plane magnetic field. Every component of this matrix can be written in terms of its Fourier components as

$$U_{\sigma\sigma'}(\vec{r}) = \sum_{\vec{K}} e^{i\vec{K}\cdot\vec{r}} U_{\vec{K},\sigma\sigma'} \Leftrightarrow U_{\vec{K},\sigma\sigma'} = \frac{1}{A} \int_{\text{cell}} \mathrm{d}\vec{r}\, e^{-i\vec{K}\cdot\vec{r}} U_{\sigma\sigma'}(\vec{r}), \tag{5.39}$$

with A the area of a unit cell in real space, and $\vec{K}$ being a vector of the reciprocal lattice as U has a periodicity of one unit cell. The potential term in the Schrödinger equation can then be rewritten as

$$U\psi = \sum_{\sigma'} \left(\sum_{\vec{K}} e^{i\vec{K}\cdot\vec{r}} U_{\vec{K},\sigma\sigma'} \right) \left(\sum_{\vec{q}} e^{i\vec{q}\cdot\vec{r}} c_{\vec{q},\sigma'} \right) \tag{5.40a}$$

$$= \sum_{\vec{K}\vec{q}\sigma'} e^{i(\vec{K}+\vec{q})\cdot\vec{r}} U_{\vec{K},\sigma\sigma'} c_{\vec{q},\sigma'}. \tag{5.40b}$$

Under the assumption of an infinite system the substitution $\vec{q} \to \vec{q} - \vec{K}$ can be made, leading to

$$U\psi = \sum_{\vec{K}'\vec{q}\sigma'} e^{i\vec{q}\cdot\vec{r}} U_{\vec{K}',\sigma\sigma'} c_{\vec{q}-\vec{K}',\sigma'}, \tag{5.41}$$

where $\vec{K}$ has been relabeled to $\vec{K}'$.

Together, the Schrödinger equation for this system becomes

$$\sum_{\vec{q}\sigma} e^{i\vec{q}\cdot\vec{r}} \left\{ (q_y + i\sigma q_x) c_{\vec{q},-\sigma} - E c_{\vec{q},\sigma} + \sum_{\vec{K}'\sigma'} U_{\vec{K}',\sigma\sigma'} c_{\vec{q}-\vec{K}',\sigma'} \right\} = 0. \tag{5.42}$$

As this needs to hold for any $\vec{r}$, this is equivalent to

$$(q_y + i\sigma q_x)c_{\vec{q},-\sigma} - Ec_{\vec{q},\sigma} + \sum_{\vec{K}'\sigma'} U_{\vec{K}',\sigma\sigma'} c_{\vec{q}-\vec{K}',\sigma'} = 0, \tag{5.43}$$

for any $\vec{q}$ and σ. This equation give the first hint that the Hamiltonian can be written as a system of linear equations but the vectors $\vec{q}$ are not the desired components. The equations can be rewritten in terms of reciprocal lattice vectors just as the potential U can be defined in terms of those. To do this, I define $\vec{q} = \vec{k} - \vec{K}$ with $\vec{K}$ again a lattice vector and $\vec{k}$ a vector in the first Brillouin zone. This can be done for any reciprocal vector $\vec{q}$, leading to

$$[k_y - K_y + i\sigma(k_x - K_x)]c_{\vec{k}-\vec{K},-\sigma} - Ec_{\vec{k}-\vec{K},\sigma} + \sum_{\vec{K}'\sigma'} U_{\vec{K}',\sigma\sigma'} c_{\vec{k}-\vec{K}-\vec{K}',\sigma'} = 0. \tag{5.44}$$

Note that $\vec{k}$ is, unlike in the previous subsection, the Bloch momentum of the particle. Substituting $\vec{K}' \to \vec{K}' - \vec{K}$ leads to

$$[k_y - K_y + i\sigma(k_x - K_x)]c_{\vec{k}-\vec{K},-\sigma} - Ec_{\vec{k}-\vec{K},\sigma} + \sum_{\vec{K}'\sigma'} U_{\vec{K}'-\vec{K},\sigma\sigma'} c_{\vec{k}-\vec{K}',\sigma'} = 0. \tag{5.45}$$

This form of the equation can be turned into a matrix-vector equation for every $\vec{k}$ in the first Brillouin zone as it only depends on $\vec{k}$ and the reciprocal lattice vectors $\vec{K}$ and $\vec{K}'$, which are discrete. The matrix is given by

$$M_{\vec{K}\sigma\vec{K}'\sigma'}(\vec{k}) = [k_y - K_y + i\sigma(k_x - K_x)]\delta_{\vec{K}\vec{K}'}(1 - \delta_{\sigma\sigma'}) + U_{\vec{K}'-\vec{K},\sigma\sigma'}, \tag{5.46}$$

such that

$$\sum_{\vec{K}'\sigma'} M_{\vec{K}\sigma\vec{K}'\sigma'}(\vec{k})\; c_{\vec{K}'\sigma'}(\vec{k}) = Ec_{\vec{K}\sigma}(\vec{k}), \tag{5.47}$$

for any $\vec{K}$ and σ, which can also be written as

$$M(\vec{k}) \cdot c(\vec{k}) = Ec(\vec{k}). \tag{5.48}$$

In this form it is clearly an eigenvalue equation. As a result, the energies E for every $\vec{k}$ are given by the eigenvalues of the matrix $M(\vec{k})$ defined by equation (5.46). The eigenvectors $c(\vec{k})$ can be interpreted as the Fourier transform of the two spin components of the periodic function $u(\vec{r})$ from equation (5.33). As such, the wave function $\psi(\vec{r})$ of a single unit cell is retrieved, up to a phase factor, by Fourier transforming the spin components of c back to real space and inserting in equation (5.33).

In theory, there is an infinite number of bands in an infinite system, but using this method the number of bands depends on the size of the matrix. The dimensions of the matrix M are defined by the number of $\vec{K}$-vectors taken into account. In a quasi-1D system, $\vec{K}$ is limited to the x-axis. When considering a system with $\vec{K}$ up to the n-th reciprocal lattice site in positive and negative x-directions, $N = 2n + 1$ different values of K_x need to be considered, ranging from $-n$ to $+n$ times the lattice vector in the x-direction. The M-matrix will then have dimensions $2N \times 2N$ because there are 2 spin components and as a result, the eigensystem will consist of $2N$ bands.
In a 2D system with square geometry, $\vec{K}$ can take $N \times N$ values, and the M-matrix will have $2N^2 \times 2N^2$ components resulting in $2N^2$ bands.

As an example, the matrix for a quasi-1D system for $N = 3$, meaning 6 bands, with an (electrostatic) potential that does not act on spin, is given by

$$M = \begin{pmatrix} U_0 & k_y+i(k_x-2\pi/l) & U_1 & 0 & U_2 & 0 \\ k_y-i(k_x-2\pi/l) & U_0 & 0 & U_1 & 0 & U_2 \\ U_{-1} & 0 & U_0 & k_y+ik_x & U_1 & 0 \\ 0 & U_{-1} & k_y-ik_x & U_0 & 0 & U_1 \\ U_{-2} & 0 & U_{-1} & 0 & U_0 & k_y+i(k_x+2\pi/l) \\ 0 & U_{-2} & 0 & U_{-1} & k_y-i(k_x+2\pi/l) & U_0 \end{pmatrix}, \tag{5.49}$$

with U_n being the n-th Fourier component of the quasi-1D potential.

On the diagonal one finds 2×2 blocks each containing a kinetic term describing one band. The elements outside these blocks represent interactions between bands that cause avoided crossings if nonzero. In order to describe a band accurately, it is thus necessary to include all bands in the calculation whose energies are close to the band under consideration. This determines the minimum size of the matrix necessary for accurate calculations. I will discuss the role of the U_0 later in section 5.2.5; it will appear that for other types of potentials the 0th Fourier component can also cause an avoided crossing.

Not only the band structure can be determined this way, also the density of states (DOS): the number of states available to electrons at a given energy, which is related to the slope of the bands. In two dimensions, minima and maxima of a band will show in the DOS as a step, while saddle points in a band will show up in the DOS as a peak. Such points are known as Van Hove singularities [84, pp. 101–103].

5.2.3 Results for quasi-1D

To verify the results I have calculated the band structure of a quasi-1D system with the potential shown in figure 5.8, using the same parameters used by Barbier et al. [13], in two different ways. The results can be seen in figure 5.9. As the surface states are Dirac fermions, positive and negative energy states exist, mirroring each other - forming infinitely many bands in the limit of an infinite crystal. Therefore the bands of interest are those in the centre of the spectrum, close to the Fermi energy. In the Bloch method, every eigenvalue represents a band and thus one can easily plot a specific band; in the transfer matrix method, small sections of higher and lower bands will be seen if they fall within the same energy range.

What we see in this figure is that the band structure exhibits a Dirac cone at $\vec{k} = (0, 0)$ and $E = 50$ meV using either methods. The energy of this Dirac point is equal to the zeroth Fourier component of the potential: the potential averaged over one unit cell. If the potential is shifted to have valleys of -50 meV and barriers of 50 meV, I find that the spectrum will be shifted 50 meV downwards and the crossing is again at zero. I will come back to the role of the 0th Fourier component when studying 2D systems in section 5.2.5.

This Dirac point can be compared to the Klein tunnelling measured in systems of one barrier. In a system with one barrier, transmission was possible at any energy for $\phi = 0 \Leftrightarrow k_y = 0$. In this periodic system, the bands are touching each other at $k_y = 0$, which means that there are left- and right-moving energy states at any energy when incident at a right angle to the barriers. At nonzero values for k_y, we see a gap between the two

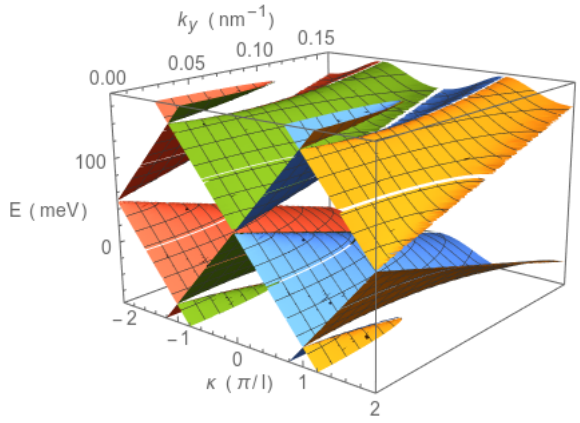

(a) Transfer matrix method. The four colours represent the four different solutions to the cosine in equation (5.36) in the interval $-2\pi/l < \kappa < 2\pi/l$.

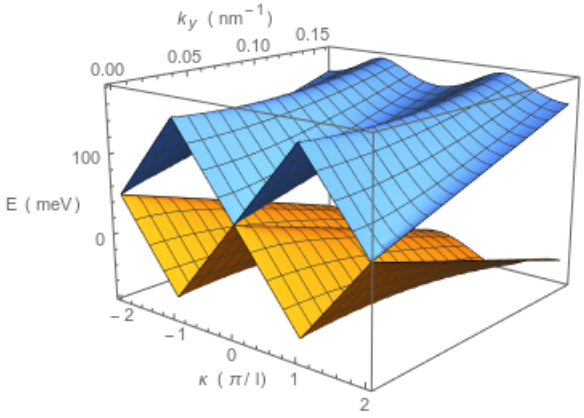

(b) Bloch method, for $N = 3$ reciprocal lattice sites, which means 6 bands. Only two innermost bands shown.

Figure 5.9: Band structure between $E = -50$ meV and $E = 150$ meV for $w = 10$ nm, $l = 20$ nm, $v_F = 10^6$ m/s, and $V = 100$ meV. Note that the interval on the x-axis is larger than the first Brillouin zone.

bands and no transmission at energies close to 50 meV. This is similar to the case of one barrier, where there was limited transmission at higher angles for energies close to the height of the potential.

Apart from some small numerical artifacts in figure 5.9a, the two are in good agreement with each other and Barbier et al. [13].

5.2.4 Results for 2D: muffin tin

To study two dimensions, I have taken the muffin tin potential on a square lattice as studied numerically by Park et al. [85]: a square lattice with a lattice constant of 10 nm, with at the centre of every unit cell a potential of 300 meV with a radius of 2.5 nm, and $v_F = 10^6$ m/s as for graphene. The unit cell of the potential can be seen in figure 5.10a and the first Brillouin zone with the Γ, X, and M high-symmetry points in figure 5.10b.

I have plotted the band structure and DOS using $N = 3$ reciprocal lattice sites in the x- and y-direction to build the matrix, for different types of potential with the same muffin tin shape in a square lattice. I have found this to be sufficient to calculate the bands close to zero energy accurately. The results can be seen in figure 5.11 without potential, figure 5.12 with electrostatic potential and figure 5.13 with an out-of-plane magnetic field.

The dimensions of this matrix are $2N^2 \times 2N^2 = 18 \times 18$. This means that there are 18 bands included in the calculation, 9 above zero energy and 9 below (unless shifted by an electrostatic potential). The result is that the density of states, in theory V-shaped, drops off rapidly above 700 meV and below -700 meV as further bands are not included in the calculation. This way the low-energy behaviour can be captured. The highest bands in the plots are not exact because they might show avoided crossings with even higher bands, if those are included.

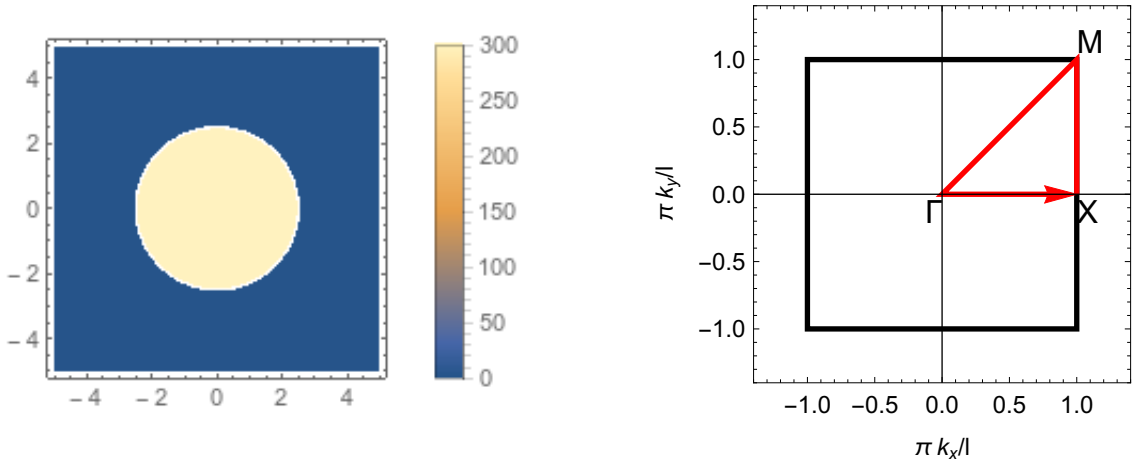

(a) Unit cell of muffin-tin potential on a square lattice. Scale in nm, colour: potential in meV.

(b) First Brillouin zone with high-symmetry points.

Figure 5.10: Unit cell and first Brillouin zone of the square lattice with a muffin-tin potential.

Electrostatic potential

What we see when comparing figures 5.11 and 5.12, is that an electrostatic potential shifts the Dirac point at the Γ point to a higher energy. At higher energies, the potential lifts some degeneracies. From the density of states, it can be seen that there is a small particle-hole asymmetry in this case. I find that the Dirac point which was at zero energy has moved to 61 meV, and the Fermi velocity given by the slope of the band near the crossing has reduced to $95.20 \pm 0.04\%$ of the original $v_F = 10^6$ m/s. I have determined this Fermi velocity using a linear fit through the energy as a function of $|\vec{k}|$ within $0.05\pi/L$ of the Dirac point. This is very similar to the quasi-1D case shown in section 5.2.3, where the Dirac cone also shifted. From the densities of states plotted here, it is even more apparent that there is an energy level where transmission tends to a minimum, like we saw in the case of a single barrier in section 5.1.1.

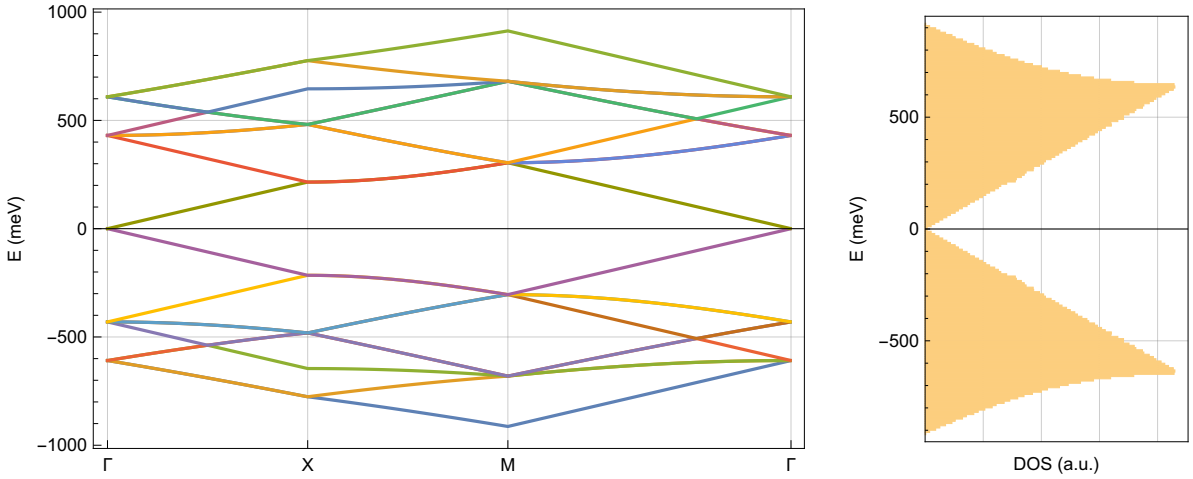

(a) Band structure (b) DOS

Figure 5.11: Band structure and DOS of TI surface states without applied potential, using $N = 3$ reciprocal lattice sites in both directions.

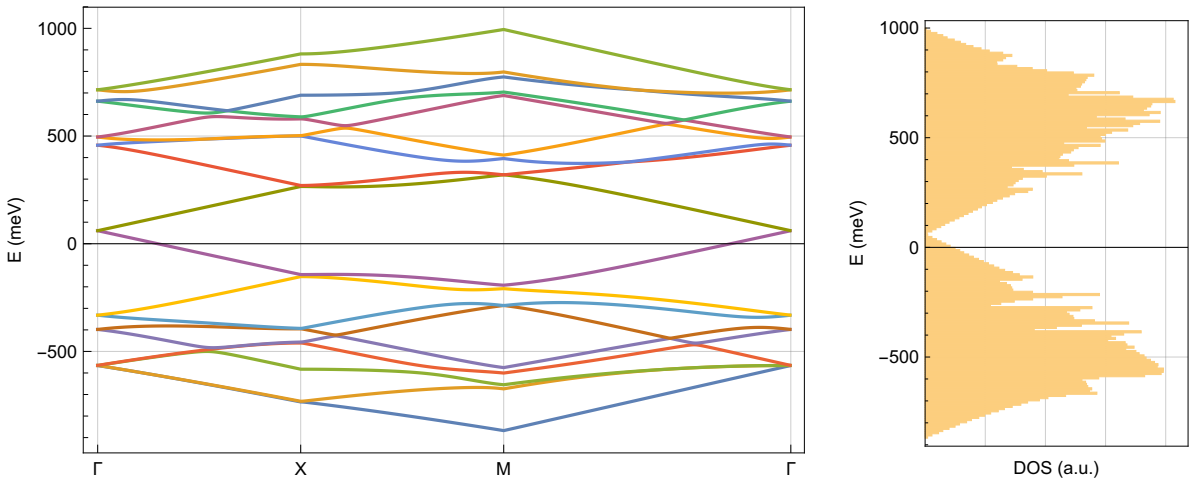

(a) Band structure (b) DOS

Figure 5.12: Band structure and DOS of TI surface states with electrostatic potential of 300 meV, using $N = 3$ reciprocal lattice sites in both directions.

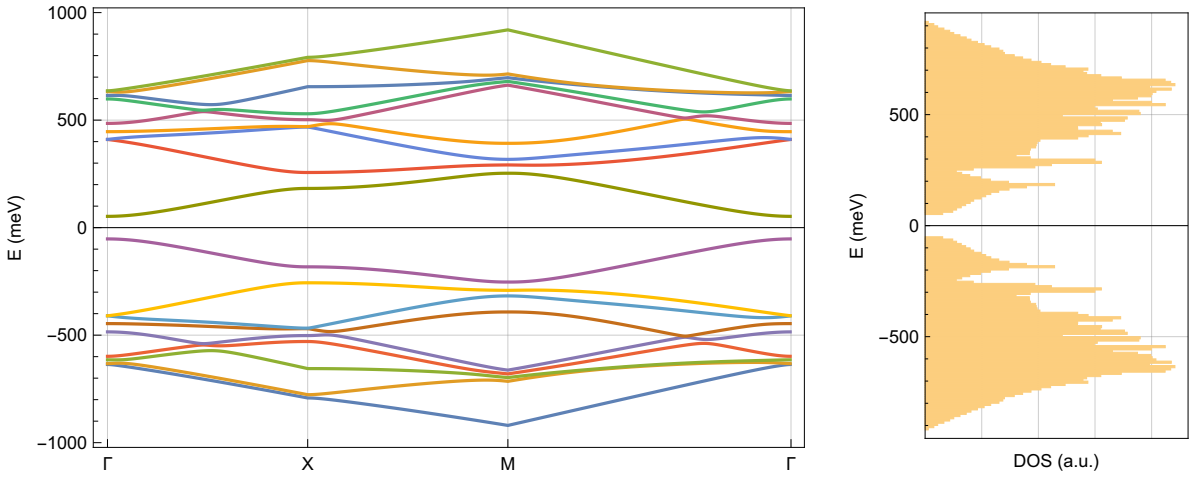

(a) Band structure (b) DOS

Figure 5.13: Band structure and DOS of TI surface states with $mB_z = 300$ meV, using $N = 3$ reciprocal lattice sites in both directions.

Out-of-plane magnetic field

As discussed in the beginning of this chapter, an out-of-plane magnetic field couples the two spin states. We see that this leads to avoided crossings in the band structure, with the biggest gap at zero energy. This is in line with the results for a a single barrier as discussed in section 5.1.2, where $|E - V| < mB_z$ lead to an exponentially decaying wave function and reduced transmission. In the limit of an infinite system this means that no transmission is possible, thus a periodic system does not have any energy states in that range: a band gap. The gap is smaller than $2mB_z$ though because of the shape of the muffin-tin potential, whose barriers do not extend infinitely in the y-direction.
Looking at the density of states we see that the Van Hove singularities become more pronounced, and no particle-hole asymmetry is observed in this system with zero electrostatic potential. I find a width of the gap of 105 meV.

In-plane magnetic field

In section 5.1.3, I discussed that a magnetic field in the x-direction in a quasi-1D system shifts the y-momentum and thus the angle of maximum transmission. In this periodic system I find that the Dirac cone in this system shifts in the $-k_y$-direction under such a field. I have plotted the band structure for $mB_x = 300$ meV in figure 5.14 as an example, where the Dirac point is located near $k_y = -0.27\pi/l$ and the Fermi velocity in has reduced to $95.32 \pm 0.23\%$ of the original $v_F = 10^6$ m/s. This is very close (within 1σ) to the value found for an equally strong electrostatic potential, which also shifted the Dirac point but did not open a gap.

I find that the Dirac point moves linearly in k-space as a function of mB_x. This is plotted in figure 5.15.

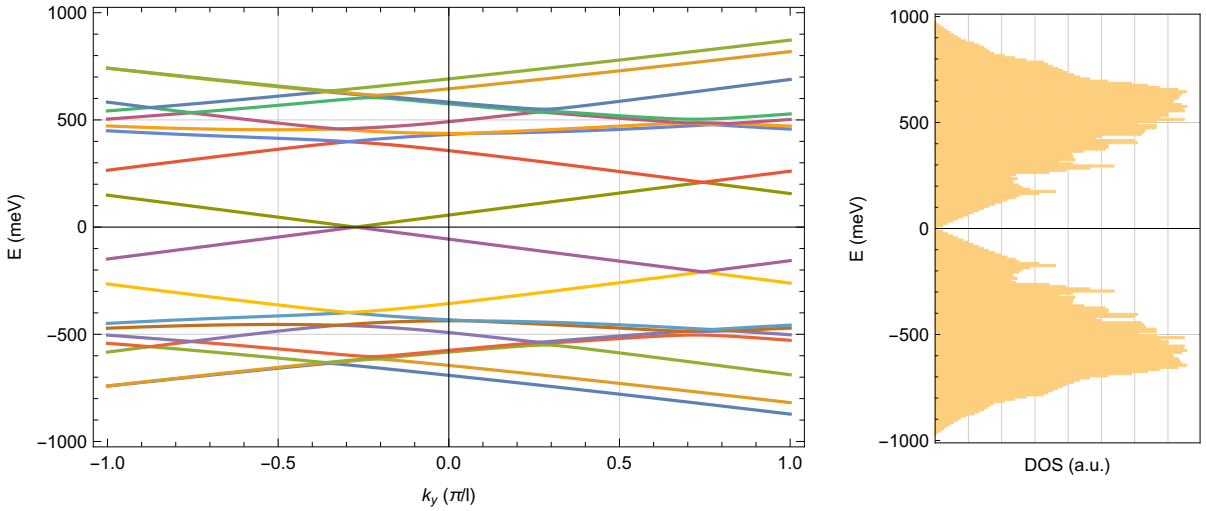

(a) Band structure

(b) DOS

Figure 5.14: Band structure along the k_y-axis of the Brillouin zone and DOS of TI surface states with $mB_x = 300$ meV, using $N = 3$ reciprocal lattice sites in both directions. The horizontal axis is different from previous figures to show the shift of the Dirac point away from the Γ point.

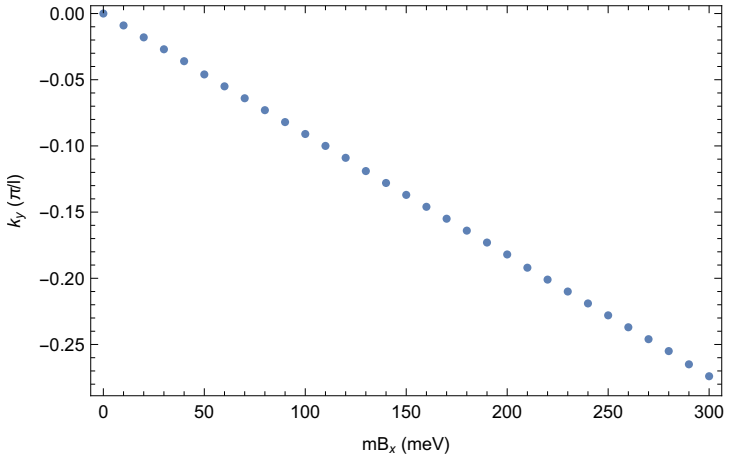

Figure 5.15: Position of Dirac points on the k_y-axis of the Brillouin zone as a function of magnetic field in the x-direction.

5.2.5 The role of the 0th Fourier component

The interesting range of the spectrum to study is close to zero energy, as the higher and lower bands in an experimental 3D TI may be obscured by the bulk's valence or conduction band. In this section I will discuss the innermost two bands, whose crossing is described by the $\vec{K} = 0$ components of the matrix. These components form a 2×2 block similar to the matrix in equation (5.5), but containing the average values of each potential over one unit cell. This part of the matrix determines whether the two innermost bands cross at a Dirac point or avoid each other, and whether the Dirac point is shifted away from zero energy in the Γ point of the Brillouin zone.

The matrix $M(\vec{k})$ of the 0th Fourier components of the various potentials is given by

$$M(\vec{k}) = \begin{pmatrix} V_0 + mB_{z,0} & (\hbar v_F k_y + mB_{x,0}) + i(\hbar v_F k_x - mB_{y,0}) \\ (\hbar v_F k_y + mB_{x,0}) - i(\hbar v_F k_x - mB_{y,0}) & V_0 - mB_{z,0} \end{pmatrix}, \tag{5.50}$$

with the 0 subscripts used to denote the $\vec{K} = 0$ Fourier component. As the muffin tin potential covers $\pi/16 \approx 20\%$ of the area in the example with $l = 10$ nm and $r = 2.5$ nm, these 0th components are given by $\pi/16$ times the applied potential.

The eigenvalues of this matrix are given by

$$E_0(k_x, k_y) = V_0 \pm \sqrt{(\hbar v_F k_y + mB_{x,0})^2 + (\hbar v_F k_x - mB_{y,0})^2 + (mB_{z,0})^2}. \tag{5.51}$$

This indicates that there is a Dirac point at $\vec{k} = (mB_{y,0}, -mB_{x,0})/\hbar v_F$, $E = V_0$ if $mB_{z,0} = 0$. For $mB_{z,0} \neq 0$, a gap of width $\Delta E = 2mB_{z,0}$ opens at this point.

In this low-energy approximation, the Dirac point in the electrostatic case is predicted to be at $E = \pi V/16 \approx 59$ meV which corresponds well with the 61 meV found in section 5.1.1. The width of the gap in the out-of-plane magnetic case is predicted to be $E = 2\pi mB_z/16 \approx 118$ meV which is a bit larger than the gap of 105 meV found in section 5.1.2. Likely this gap becomes smaller due to coupling to higher bands, as it can be seen in figure 5.13 that the crossings with the next bands are avoided. The location in k-space of the Dirac point at zero energy in the in-plane magnetic case is predicted to be $k_y = -\pi mB_x/16\hbar v_F \approx -0.27\pi/l$, which matches the value found in section 5.1.3.

These results indicate that the position of the Dirac point and the presence of a gap can be well predicted using just the average value of the potential. This suggests that a potential with an average of zero does not move the Dirac point or open a gap: potentials consisting of (positive) barriers and (negative) wells. In such a case the two innermost energy bands do not couple to each other, though they will couple to higher energy bands.

As a test, I have calculated the band structure for an out-of-plane magnetic field, shifted such that its average value is zero. The barrier is still 300 meV higher than the valley. The result can be seen in figure 5.16. It can be seen that there is no gap at zero energy, even though the avoided crossings at higher energies remain. The Fermi velocity is reduced more strongly to $89.4 \pm 0.6\%$ of its original value.

I conclude that the 0th Fourier component, or average value of the potential, can predict accurately where the Dirac point is found and whether there is a gap. On the other hand, the size of the gap is overestimated by about 12% in the example and the reduction in

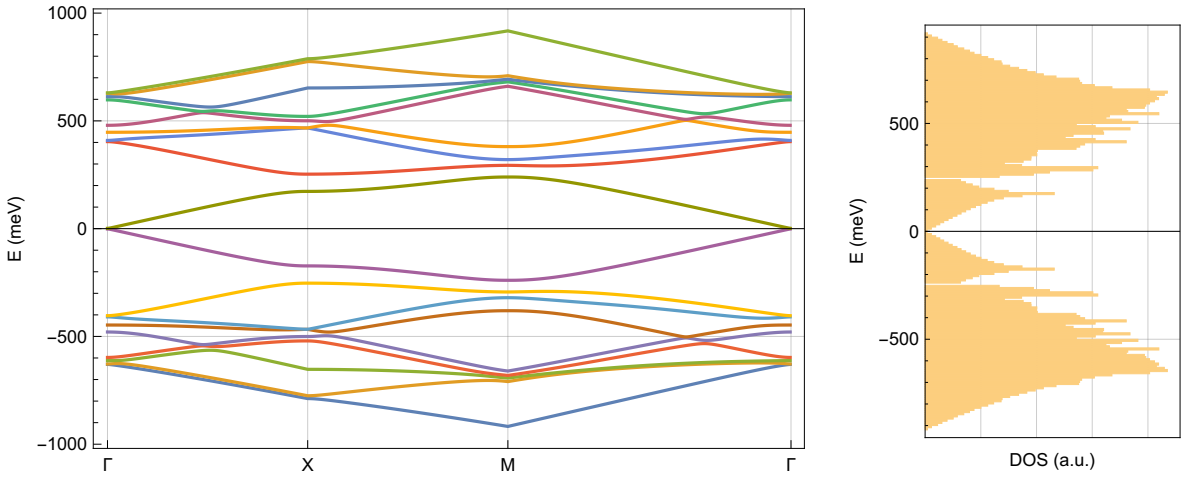

(a) Band structure

(b) DOS

Figure 5.16: Band structure and DOS of TI surface states with a barrier of height $mB_z = 300$ meV and the average value of the potential set to 0, up to the 1st Fourier components of the potential.

Fermi velocity cannot be modelled using equation (5.51), which gives a Fermi velocity equal to the original v_F in any case without a gap. I conclude that, while the location of the Dirac point is given by the average of the potential, the Fermi velocity near this point is determined by the higher Fourier components which describe the shape of the potential.

Chapter 6

Conclusions and outlook

It is known that electrons can exhibit multifractality close to an Anderson localisation transition [8], and an example of such a system where multifractality has been observed is a quantum Hall system close to the Landau level transition [9]. The electronic states in the third generation of a Sierpiński triangle which I studied in chapter 4, on the other hand, do not form a multifractal. This is a nice result in the sense that it provides new evidence to support the conclusion of Kempkes et al. [4] that fractality can be replicated using electronic states.

Surface states of 3D topological insulators, as discussed in chapter 5, are a promising material to build quantum simulators. I have started with a single barrier and observed Klein tunnelling for electrostatic and in-plane magnetic barriers; in a periodic system with one of these potentials, there is a Dirac point which is moved away from zero energy by an electrostatic potential or away from the Γ point by an in-plane magnetic field. Out-of-plane magnetic fields kill Klein tunnelling in the case of a single barrier, and open a gap in the case of a periodic system. Interestingly, many of the properties of a periodic system can be derived from the average value of the potential (or 0th Fourier component) rather than its exact shape.

What will depend on the shape of the potential, is the local density of states (LDOS). On copper surfaces, the LDOS has been used to study confinement to lattice sites. A possible next step would be to study this on topological insulator surfaces too for various lattices. Another suggestion for future research would be to classify the surface states using topological quantum chemistry [86], which has already been done with photonic systems [87].

Acknowledgements

I would like to thank my supervisors, Cristiane Morais Smith, Sander Kempkes and Dario Bercioux, for helping me to make this project possible, and my colleagues in the research groups in Utrecht and San Sebastián for many useful discussions. In particular, I would like to thank Ward Vleeshouwers for useful discussions about multifractality and María Blanco de Paz for discussions about topological quantum chemistry, which offers possibilities for future research, and Mikael Fremling for helping me with the implementation of the box counting procedure.

Bibliography

[1] K. K. Gomes, W. Mar, W. Ko, F. Guinea, and H. C. Manoharan, "Designer Dirac fermions and topological phases in molecular graphene," *Nature*, vol. 483, pp. 306–310, 2012.

[2] M. R. Slot, T. S. Gardenier, P. H. Jacobse, G. C. P. van Miert, S. N. Kempkes, S. J. M. Zevenhuizen, C. Morais Smith, D. Vanmaekelbergh, and I. Swart, "Experimental realization and characterization of an electronic Lieb lattice," *Nature Physics*, vol. 13, pp. 672–676, 2017.

[3] M. R. Slot, S. N. Kempkes, E. J. Knol, W. M. J. van Weerdenburg, J. J. van den Broeke, D. Wegner, D. Vanmaekelbergh, A. A. Khajetoorians, C. Morais Smith, and I. Swart, "p-band engineering in artificial electronic lattices," *Phys. Rev. X*, vol. 9, p. 011009, 2019.

[4] S. N. Kempkes, M. R. Slot, S. E. Freeney, S. J. M. Zevenhuizen, D. Vanmaekelbergh, I. Swart, and C. Morais Smith, "Design and characterization of electrons in a fractal geometry," *Nature Physics*, vol. 15, pp. 127–131, 2018.

[5] E. van Veen, S. Yuan, M. I. Katsnelson, M. Polini, and A. Tomadin, "Quantum transport in Sierpinski carpets," *Phys. Rev. B*, vol. 93, p. 115428, 2016.

[6] M. Brzezińska, A. M. Cook, and T. Neupert, "Topology in the Sierpiński-Hofstadter problem," *Phys. Rev. B*, vol. 98, p. 205116, 2018.

[7] M. Fremling, M. van Hooft, C. Morais Smith, and L. Fritz, "A Chern insulator in $\ln(8)/\ln(3)$ dimensions," *arXiv preprint arXiv:1906.07387*, 2019.

[8] F. Evers and A. D. Mirlin, "Anderson transitions," *Reviews of Modern Physics*, vol. 80, no. 4, p. 1355, 2008.

[9] M. Morgenstern, J. Klijn, C. Meyer, and R. Wiesendanger, "Real-space observation of drift states in a two-dimensional electron system at high magnetic fields," *Phys. Rev. Lett.*, vol. 90, p. 056804, 2003.

[10] H. Zhang, C.-X. Liu, X.-L. Qi, X. Dai, Z. Fang, and S.-C. Zhang, "Topological insulators in Bi_2Se_3, Bi_2Te_3 and Sb_2Te_3 with a single Dirac cone on the surface," *Nature Physics*, vol. 5, pp. 438–442, 2009.

[11] D. Hsieh, Y. Xia, D. Qian, L. Wray, J. H. Dil, F. Meier, J. Osterwalder, L. Patthey, J. G. Checkelsky, N. P. Ong *et al.*, "A tunable topological insulator in the spin helical Dirac transport regime," *Nature*, vol. 460, pp. 1101–1105, 2009.

[12] M. I. Katsnelson, K. S. Novoselov, and A. K. Geim, "Chiral tunnelling and the Klein paradox in graphene," *Nature Physics*, vol. 2, pp. 620–625, 2006.

[13] M. Barbier, F. M. Peeters, P. Vasilopoulos, and J. M. Pereira Jr., "Dirac and Klein-Gordon particles in one-dimensional periodic potentials," *Phys. Rev. B*, vol. 77, p. 115446, 2008.

[14] M. Barbier, P. Vasilopoulos, and F. M. Peeters, "Dirac electrons in a Kronig-Penney potential: Dispersion relation and transmission periodic in the strength of the barriers," *Phys. Rev. B*, vol. 80, p. 205415, 2009.

[15] L. Lenz and D. Bercioux, "Dirac-Weyl electrons in a periodic spin-orbit potential," *Europhysics Letters*, vol. 96, no. 2, p. 27006, 2011.

[16] B. D. Kong, Y. G. Semenov, C. M. Krowne, and K. W. Kim, "Unusual magnetoresistance in a topological insulator with a single ferromagnetic barrier," *Applied Physics Letters*, vol. 98, p. 243112, 2011.

[17] R. P. Feynman, "Simulating physics with computers," *International journal of theoretical physics*, vol. 21, no. 6-7, pp. 467–488, 1982.

[18] I. M. Georgescu, S. Ashhab, and F. Nori, "Quantum simulation," *Reviews of Modern Physics*, vol. 86, no. 1, pp. 153–185, 2014.

[19] J. Ignacio Cirac and P. Zoller, "Goals and opportunities in quantum simulation," *Nature Physics*, vol. 8, pp. 264–266, 2012.

[20] J. Yang and Z. H. Musslimani, "Fundamental and vortex solitons in a two-dimensional optical lattice," *Optics letters*, vol. 28, pp. 2094–2096, 2003.

[21] P. S. Jessen and I. H. Deutsch, "Optical lattices," in *Advances in Atomic, Molecular, and Optical Physics*. Elsevier, 1996, vol. 37, pp. 95–138.

[22] I. Bloch, J. Dalibard, and W. Zwerger, "Many-body physics with ultracold gases," *Reviews of modern physics*, vol. 80, pp. 885–964, 2008.

[23] I. Bloch, J. Dalibard, and S. Nascimbene, "Quantum simulations with ultracold quantum gases," *Nature Physics*, vol. 8, pp. 267–276, 2012.

[24] L. Mazza, A. Bermudez, N. Goldman, M. Rizzi, M. A. Martin-Delgado, and M. Lewenstein, "An optical-lattice-based quantum simulator for relativistic field theories and topological insulators," *New Journal of Physics*, vol. 14, p. 015007, 2012.

[25] L. Sanchez-Palencia, D. Clément, P. Lugan, P. Bouyer, G. V. Shlyapnikov, and A. Aspect, "Anderson localization of expanding Bose-Einstein condensates in random potentials," *Physical Review Letters*, vol. 98, p. 210401, 2007.

[26] F. Jendrzejewski, A. Bernard, K. Mueller, P. Cheinet, V. Josse, M. Piraud, L. Pezzé, L. Sanchez-Palencia, A. Aspect, and P. Bouyer, "Three-dimensional localization of ultracold atoms in an optical disordered potential," *Nature Physics*, vol. 8, pp. 398–403, 2012.

[27] R. Blatt and C. F. Roos, "Quantum simulations with trapped ions," *Nature Physics*, vol. 8, pp. 277–284, 2012.

[28] E. Zohar, J. I. Cirac, and B. Reznik, "Quantum simulations of lattice gauge theories using ultracold atoms in optical lattices," *Reports on Progress in Physics*, vol. 79, p. 014401, 2015.

[29] X.-s. Ma, B. Dakic, W. Naylor, A. Zeilinger, and P. Walther, "Quantum simulation of the wavefunction to probe frustrated Heisenberg spin systems," *Nature Physics*, vol. 7, pp. 399–405, 2011.

[30] A. Aspuru-Guzik and P. Walther, "Photonic quantum simulators," *Nature Physics*, vol. 8, pp. 285–291, 2012.

[31] M. C. Rechtsman, J. M. Zeuner, Y. Plotnik, Y. Lumer, D. Podolsky, F. Dreisow, S. Nolte, M. Segev, and A. Szameit, "Photonic Floquet topological insulators," *Nature*, vol. 496, pp. 196–200, 2013.

[32] M. Hafezi, S. Mittal, J. Fan, A. Migdall, and J. M. Taylor, "Imaging topological edge states in silicon photonics," *Nature Photonics*, vol. 7, pp. 1001–1005, 2013.

[33] A. Tadjine, "Structure et propriétés de réseaux cohérents de nanocristaux semiconducteurs," PhD thesis, University of Lille, 2018.

[34] E. Kalesaki, C. Delerue, C. Morais Smith, W. Beugeling, G. Allan, and D. Vanmaekelbergh, "Dirac cones, topological edge states, and nontrivial flat bands in two-dimensional semiconductors with a honeycomb nanogeometry," *Phys. Rev. X*, vol. 4, p. 011010, 2014.

[35] M. P. Boneschanscher, W. H. Evers, J. J. Geuchies, T. Altantzis, B. Goris, F. T. Rabouw, S. A. P. van Rossum, H. S. J. van der Zant, L. D. A. Siebbeles, G. van Tendeloo *et al.*, "Long-range orientation and atomic attachment of nanocrystals in 2D honeycomb superlattices," *Science*, vol. 344, pp. 1377–1380, 2014.

[36] W. Beugeling, E. Kalesaki, C. Delerue, Y.-M. Niquet, D. Vanmaekelbergh, and C. Morais Smith, "Topological states in multi-orbital HgTe honeycomb lattices," *Nature Communications*, vol. 6, p. 6316, 2015.

[37] C.-H. Park and S. G. Louie, "Making massless Dirac fermions from a patterned two-dimensional electron gas," *Nano letters*, vol. 9, pp. 1793–1797, 2009.

[38] G. De Simoni, A. Singha, M. Gibertini, B. Karmakar, M. Polini, V. Piazza, L. N. Pfeiffer, K. W. West, F. Beltram, and V. Pellegrini, "Delocalized-localized transition in a semiconductor two-dimensional honeycomb lattice," *Applied Physics Letters*, vol. 97, p. 132113, 2010.

[39] M. Gibertini, A. Singha, V. Pellegrini, M. Polini, G. Vignale, A. Pinczuk, L. N. Pfeiffer, and K. W. West, "Engineering artificial graphene in a two-dimensional electron gas," *Phys. Rev. B*, vol. 79, p. 241406, 2009.

[40] L. Nádvorník, M. Orlita, N. A. Goncharuk, L. Smrčka, V. Novák, V. Jurka, K. Hruška, Z. Výborný, Z. R. Wasilewski, M. Potemski, and K. Výborný, "From laterally modulated two-dimensional electron gas towards artificial graphene," *New Journal of Physics*, vol. 14, p. 053002, 2012.

[41] D. Scarabelli, S. Wang, A. Pinczuk, S. J. Wind, Y. Y. Kuznetsova, L. N. Pfeiffer, K. West, G. C. Gardner, M. J. Manfra, and V. Pellegrini, "Fabrication of artificial graphene in a GaAs quantum heterostructure," *Journal of Vacuum Science & Technology B*, vol. 33, p. 06FG03, 2015.

[42] R. Drost, T. Ojanen, A. Harju, and P. Liljeroth, "Topological states in engineered atomic lattices," *Nature Physics*, vol. 13, pp. 668–671, 2017.

[43] D. Bercioux and S. Otte, "Quantum simulation: Solid-state platforms," *Nature Physics*, vol. 13, pp. 628–629, 2017.

[44] X. Dai, T. L. Hughes, X.-L. Qi, Z. Fang, and S.-C. Zhang, "Helical edge and surface states in HgTe quantum wells and bulk insulators," *Phys. Rev. B*, vol. 77, p. 125319, 2008.

[45] L. Fu, C. L. Kane, and E. J. Mele, "Topological insulators in three dimensions," *Phys. Rev. Lett.*, vol. 98, p. 106803, 2007.

[46] J. Honolka, A. A. Khajetoorians, V. Sessi, T. O. Wehling, S. Stepanow, J.-L. Mi, B. B. Iversen, T. Schlenk, J. Wiebe, N. B. Brookes *et al.*, "In-plane magnetic anisotropy of Fe atoms on Bi_2Se_3(111)," *Phys. Rev. Lett.*, vol. 108, p. 256811, 2012.

[47] T. Schlenk, M. Bianchi, M. Koleini, A. Eich, O. Pietzsch, T. O. Wehling, T. Frauenheim, A. Balatsky, J.-L. Mi, B. B. Iversen *et al.*, "Controllable magnetic doping of the surface state of a topological insulator," *Phys. Rev. Lett.*, vol. 110, p. 126804, 2013.

[48] M. Scheid, D. Bercioux, and K. Richter, "Zeeman ratchets: pure spin current generation in mesoscopic conductors with non-uniform magnetic fields," *New Journal of Physics*, vol. 9, no. 11, p. 401, 2007.

[49] M. Scheid, A. Pfund, D. Bercioux, and K. Richter, "Coherent spin ratchets: A spin-orbit based quantum ratchet mechanism for spin-polarized currents in ballistic conductors," *Phys. Rev. B*, vol. 76, p. 195303, 2007.

[50] L. Bürgi, L. Petersen, H. Brune, and K. Kern, "Noble metal surface states: deviations from parabolic dispersion," *Surface science*, vol. 447, pp. L157–L161, 2000.

[51] J. Kröger, L. Limot, H. Jensen, R. Berndt, and P. Johansson, "Stark effect in Au(111) and Cu(111) surface states," *Phys. Rev. B*, vol. 70, p. 033401, 2004.

[52] V. J. Emery, "Theory of high-T_c superconductivity in oxides," *Phys. Rev. Lett.*, vol. 58, pp. 2794–2797, 1987.

[53] N. W. Ashcroft and N. D. Mermin, *Solid State Physics*. Saunders College Publishing, 1976.

[54] H. Steinhaus, "Length, shape and area," in *Colloq. Math.*, vol. 3, 1954, pp. 1–13.

[55] B. Mandelbrot, "How long is the coast of Britain? Statistical self-similarity and fractional dimension," *Science*, vol. 156, pp. 636–638, 1967.

[56] F. Hausdorff, "Dimension und äußeres Maß," *Mathematische Annalen*, vol. 79, no. 1-2, pp. 157–179, 1918.

[57] B. B. Mandelbrot, *The fractal geometry of nature*. WH Freeman New York, 1982.

[58] K. Falconer, *Fractal geometry: mathematical foundations and applications*. John Wiley & Sons, 2004.

[59] M. Shishikura, "The Hausdorff dimension of the boundary of the Mandelbrot set and Julia sets," *Annals of Mathematics*, pp. 225–267, 1998.

[60] W. Sierpiński, "Sur une courbe dont tout point est un point de ramification," *Compte Rendus hebdomadaires des séances de l'Académie des sciences*, vol. 160, pp. 302–305, 1915.

[61] E. Conversano and L. T. Lalli, "Sierpinski triangles in stone, on medieval floors in Rome," *J. Appl. Math*, vol. 4, pp. 114–122, 2011.

[62] L. R. Meza, A. J. Zelhofer, N. Clarke, A. J. Mateos, D. M. Kochmann, and J. R. Greer, "Resilient 3D hierarchical architected metamaterials," *Proceedings of the National Academy of Sciences*, vol. 112, no. 37, pp. 11 502–11 507, 2015.

[63] F. J. Dyson, "The search for extraterrestrial technology," in *Perspectives in modern physics*. John Wiley & Sons, New York, 1966, pp. 641–655.

[64] R. Lopes and N. Betrouni, "Fractal and multifractal analysis: a review," *Medical image analysis*, vol. 13, pp. 634–649, 2009.

[65] A. N. D. Posadas, D. Giménez, M. Bittelli, C. M. P. Vaz, and M. Flury, "Multifractal characterization of soil particle-size distributions," *Soil Science Society of America Journal*, vol. 65, pp. 1361–1367, 2001.

[66] M. Hénon, "A two-dimensional mapping with a strange attractor," in *The Theory of Chaotic Attractors*. Springer, 1976, pp. 94–102.

[67] D. A. Russell, J. D. Hanson, and E. Ott, "Dimension of strange attractors," *Phys. Rev. Lett.*, vol. 45, pp. 1175–1178, 1980.

[68] A. Chhabra and R. V. Jensen, "Direct determination of the $f(\alpha)$ singularity spectrum," *Phys. Rev. Lett.*, vol. 62, pp. 1327–1330, 1989.

[69] T. C. Halsey, M. H. Jensen, L. P. Kadanoff, I. Procaccia, and B. I. Shraiman, "Fractal measures and their singularities: The characterization of strange sets," *Phys. Rev. A*, vol. 33, pp. 1141–1151, 1986.

[70] K. S. Novoselov, A. K. Geim, S. V. Morozov, D. Jiang, M. I. Katsnelson, I. V. Grigorieva, S. V. Dubonos, and A. A. Firsov, "Two-dimensional gas of massless Dirac fermions in graphene," *Nature*, vol. 438, no. 7065, p. 197, 2005.

[71] A. De Martino, L. Dell'Anna, and R. Egger, "Magnetic confinement of massless Dirac fermions in graphene," *Phys. Rev. Lett.*, vol. 98, p. 066802, 2007.

[72] L. Dell'Anna and A. De Martino, "Multiple magnetic barriers in graphene," *Phys. Rev. B*, vol. 79, p. 045420, 2009.

[73] D. Bercioux and A. De Martino, "Spin-resolved scattering through spin-orbit nanostructures in graphene," *Phys. Rev. B*, vol. 81, p. 165410, 2010.

[74] M. Dvorak, W. Oswald, and Z. Wu, "Bandgap opening by patterning graphene," *Scientific reports*, vol. 3, p. 2289, 2013.

[75] P. Sessi, J. R. Guest, M. Bode, and N. P. Guisinger, "Patterning graphene at the nanometer scale via hydrogen desorption," *Nano letters*, vol. 9, pp. 4343–4347, 2009.

[76] A. Sinitskii and J. M. Tour, "Patterning graphene through the self-assembled templates: toward periodic two-dimensional graphene nanostructures with semiconduc-

tor properties," *Journal of the American Chemical Society*, vol. 132, no. 42, pp. 14 730–14 732, 2010.

[77] V. Strong, S. Dubin, M. F. El-Kady, A. Lech, Y. Wang, B. H. Weiller, and R. B. Kaner, "Patterning and electronic tuning of laser scribed graphene for flexible all-carbon devices," *ACS nano*, vol. 6, no. 2, pp. 1395–1403, 2012.

[78] H. Köhler and E. Wöchner, "The g-factor of the conduction electrons in Bi_2Se_3," *physica status solidi (b)*, vol. 67, no. 2, pp. 665–675, 1975.

[79] J. Xiong, Y. Luo, Y. Khoo, S. Jia, R. J. Cava, and N. P. Ong, "High-field Shubnikov–de Haas oscillations in the topological insulator Bi_2Te_2Se," *Phys. Rev. B*, vol. 86, p. 045314, 2012.

[80] B. H. J. McKellar and G. J. Stephenson Jr., "Relativistic quarks in one-dimensional periodic structures," *Phys. Rev. C*, vol. 35, no. 6, p. 2262, 1987.

[81] S.-Y. Xu, M. Neupane, C. Liu, D. Zhang, A. Richardella, L. A. Wray, N. Alidoust, M. Leandersson, T. Balasubramanian, J. Sánchez-Barriga *et al.*, "Hedgehog spin texture and Berry's phase tuning in a magnetic topological insulator," *Nature Physics*, vol. 8, no. 8, p. 616, 2012.

[82] B. H. J. McKellar and G. J. Stephenson Jr., "Klein paradox and the Dirac-Kronig-Penney model," *Phys. Rev. A*, vol. 36, no. 6, p. 2566, 1987.

[83] S. Datta, *Electronic transport in mesoscopic systems*. Cambridge University Press, 1997.

[84] G. Grosso and G. Pastori Parravicini, *Solid State Physics*, 2nd ed. Academic Press, 2014.

[85] C.-H. Park, L. Yang, Y.-W. Son, M. L. Cohen, and S. G. Louie, "Anisotropic behaviours of massless Dirac fermions in graphene under periodic potentials," *Nature Physics*, vol. 4, no. 3, p. 213, 2008.

[86] B. Bradlyn, L. Elcoro, J. Cano, M. G. Vergniory, Z. Wang, C. Felser, M. Aroyo, and B. A. Bernevig, "Topological quantum chemistry," *Nature*, vol. 547, pp. 298–305, 2017.

[87] M. Blanco de Paz, M. G. Vergniory, D. Bercioux, A. García-Etxarri, and B. Bradlyn, "Engineering fragile topology in photonic crystals: Topological quantum chemistry of light," *arXiv preprint arXiv:1903.02562*, 2019.